Prediction of Ductile Fracture for Circular Hollow Section Bracing Members under Extremely Low Cycle Fatigue

Fei Xu[1,2], Tak-Ming Chan[1,*] Therese Sheehan[3], Leroy Gardner[4]

1. Department of Civil and Environmental Engineering, The Hong Kong Polytechnic University, Hong Kong;

2. Faculty of Engineering, Hokkaido University, Japan;

3. Faculty of Engineering and Informatics, University of Bradford, United Kingdom;

4. Department of Civil and Environmental Engineering, Imperial College London, South Kensington Campus, United Kingdom.

Abstract: The fracture behaviour of concentrically loaded circular hollow section (CHS) bracing members under extremely low cycle fatigue (ELCF) is examined in this paper. Finite element (FE) models capable of predicting fracture initiation and propagation on cyclically loaded braces were developed. A structural steel ductile fracture criterion, together with a damage accumulation rule that can account for the effects of both stress triaxiality and Lode angle, was adopted in the FE models. The FE models were validated against the available test results from different experimental programmes and shown to provide an accurate prediction of both the hysteretic response and the ELCF fracture cracking process. The coupling effects of buckling and fracture on the ELCF performance of braces were assessed through a parametric study. This parametric study examined the influences of the geometry, material and manufacturing process on the local and global deformation, and the ductility of the braces. Predictive equations for the localized strains and member ductility were proposed based on a plastic hinge model. The seismic performance of a chevron braced frame was also evaluated in terms of story drift angle according to the requirements of the current design code.

Keywords: Bracing members; Extremely low cycle fatigue; Buckling; Ductility; Fracture prediction.

*Corresponding author: tak-ming.chan@polyu.edu.hk

1. Introduction

Dissipative components play a crucial role in earthquake-resisting structures since they absorb energy through inelastic deformation, reduce the forces in other elements and enable efficient structural design. In concentrically braced frames, this dissipation is achieved by diagonal bracing members. Tubular sections are becoming increasingly prevalent because of their excellent compressive and torsional resistances, as well as visual appeal. However, the energy-dissipation performance is often compromised by fracture at the mid-length due to the occurrence of large deformations and buckling in this region.

Experimental studies on cyclically loaded bracing members (i.e. Tremblay [1], Fell [2], Nip et al. [3,4], Sheehan and Chan [5] and Elchalakani et al. [6]) has been conducted to investigate the influence of geometry, material type and manufacturing process on their hysteretic response, ductility capacity and fracture life. Fracture initiated soon after the occurrence of local buckling, due to the accumulation of high local strains, causing sudden strength loss. As a result, the prescribed ductility levels, such as the maximum inter-story drift for a braced frame, were not achieved. From previous experimental investigations [1-6], the diameter-to-thickness ratio (D/t) and member slenderness (KL/r) were found to have a major influence on the cyclic-loading-induced fracture of bracing members, where D, t, L and r are the diameter, thickness, length and radius of gyration, respectively, of the tube, and K is the effective length factor. However, quantifying the effects of these parameters on the fracture life of bracing members remains a challenge. In addition, discrepancies in ductility capacity and fracture life between braces from different manufacturing processes were observed in circular, square and rectangular hollow sections (CHS, SHS and RHS) [3,5,7]. During the seismic design of structures, an understanding of these effects would enable more informed choices to be made on member selection based on the required performance.

Currently, investigations into extremely low cycle fatigue (ELCF) induced fracture

processes mainly depend on experiments due to the lack of a reliable fracture prediction methodology. However, experiments on large-scale bracing members, which undergo significant out-of-plane deformations, are often limited by the available laboratory space and facilities. Numerical simulations are therefore becoming a popular means to examine structural problems, offering an efficient and cost-effective alternative to laboratory tests. Different fracture prediction methodologies have been developed for use in parallel with numerical simulations to predict earthquake-induced fracture at a member-level, such as: (1) the cycle counting technique through fibre-based elements [8] without consideration of buckling effects, (2) post-processing of finite element (FE) simulation data [9] using the "rain flow" counting technique in conjunction with the Coffin-Mason strain-life relationship [10,11] and (3) FE simulations with a fracture prediction model and corresponding damage evolution rule [2, 12].

The counting methodologies can only provide the number of cycles to fracture. The third approach has the potential to assess the fracture process (including initiation and propagation) and the post-fracture behaviour due to crack propagation. However, traditional fracture prediction models, such as linear-elastic and elastic-plastic fracture mechanics (LEFM and EPFM), are only valid in the following conditions [13]: (1) when fracture initiates in the vicinity of a pre-defined sharp crack, (2) when there is a limited inelastic region around the pre-defined sharp crack, and (3) under monotonic loading.

When steel materials undergo either ductile fracture or ELCF fracture, similar mechanisms are observed at both microscopic and macroscopic levels. Kanvinde and Deierlein [14] observed that the underlying mechanisms of micro-void growth and coalescence are similar for ELCF fracture and ductile fracture under monotonic loading conditions [14]. Therefore, ductile fracture models with a corresponding damage accumulation rule were adopted to predict the ELCF fracture of metals in previous investigations [15-18].

79 The ductile fracture models are generally categorized into

80 (I) Physics-based (McClintock [19], Rice-Tracey [20], Gurson [21] and Gurson-
81 Tvergaard-Needleman (GTN) [22] models);

82 (II) Phenomenological (maximum shear stress [23] and modified Mohr-Coulomb
83 model (MMC) [24,25] models) and

84 (III) Empirical (Johnson-Cook [26] Bao-Wierzbicki [27] and Xue-Wierzbicki[28]
85 models).

86 Kanvinde and Deierlein [14] proposed a physics-based prediction model named the
87 cyclic void growth model (CVGM), based on the micro-mechanism of void growth and
88 coalescence. The CVGM model assumes that fracture depends on stress triaxiality (η), which
89 is in line with the observations of McClintock [19] and Rice and Tracey [20].

90 Recently the Lode angle (θ) as defined in Fig. 1, which captures the effects of deviatoric
91 stress states, was found to have a significant influence on metal ductile fracture at low stress
92 triaxiality levels [24-25,28-30]. Barsoum and Jonas [29] conducted experiments on steel
93 fractography with the technology of a scanning electron microscope (SEM). They observed
94 different fracture mechanisms including: (1) fracture after a damage sequence of nucleation,
95 growth and coalescence of internal cavities (η = 1.10 in [29]), (2) shear band formation
96 followed by internal void shear fracture (η = 0.47 in [29]) and (3) a mixture of these two
97 failure modes at different stress triaxiality levels (η = 0.85 in [29]). It was found that at a low
98 stress triaxiality level (η = 0.47 in [29]), relatively shallow and elongated shear dimples were
99 oriented along the shear direction on the fracture surface, which indicated the strong
100 dependence of the shear stress state on the Lode angle [29]. Further research [30-34] through
101 micro-mechanical numerical simulations was conducted in the last decade to assess the
102 relationship between the macro stress state and the micro defect evolution. Results further
103 confirmed the significant influence of the Lode angle on the ductile fracture at low stress
104 triaxiality levels and the dominant role of stress triaxiality at high stress triaxiality levels.

A limitation of the CVGM model [14] stems from the fact that fracture is assumed to depend only on stress triaxiality (η)—the model fails to accurately predict ductile fracture at low stress triaxiality levels where the shear stress state has been shown to depend strongly on Lode angle [29]. However, in structural engineering, fracture typically occurs between low and intermediate stress triaxiality levels [13] where $\eta < 1.0$, such as shear fracture in the panel zone of beam-to-column connections and local buckling induced fracture of cyclically loaded braces. Researchers have proposed ductile fracture models incorporating damage evolution rules, which depend on both stress triaxiality and Lode angle [15-18,35] and these have been verified against material (coupon) - level tests. In this paper, the primary objective is to use these fracture prediction models [15-18,35] to predict the ELCF fracture of cyclically loaded bracing members, by generating numerical models, validated against experimental data from previous research. The influences of member geometry, material and manufacturing process on the deformation and failure are examined. Using plastic hinge models, a failure criterion is proposed, as a function of localized strain prior to fracture, and the seismic performance of a braced frame is assessed against the requirements of AISC 341-10 [36].

2. Existing Ductile Fracture Models under Extremely Low Cycle Fatigue

Steel structures subjected to severe earthquakes undergo significant plastic strains which cause material hardening and softening during the reversing load cycles. This leads to extremely low cycle fatigue and results in the same fracture profile and the dimple-dominated surface as that which occurs during ductile fracture under monotonic loading [14]. ELCF fracture is accompanied by large deformations and usually occurs after only a few cycles. Due to the significant non-localized plasticity that develops before fracture and the absence of pre-defined “cracks”, the validity of the conventional fracture prediction methodologies (i.e. LEFM and EPFM) is questionable [13]. Moreover, the accumulative fatigue damage

130 approach (Manson-Coffin law [10,11]) that can accurately predict fracture life under low
131 cycle fatigue (LCF) loading conditions, has been shown to over-predict fracture life under
132 ELCF loading conditions [37-39].

133 As discussed earlier, the effects of the both hydrostatic pressure and the third deviatoric
134 stress levels (expressed as a function of stress triaxiality (η) and Lode angle (θ)) are essential
135 to accurately predict fracture for low, intermediate and high stress triaxiality levels. Smith et
136 al. [35] proposed a stress-weight damage model (SWDM) to address these effects on fracture.
137 Meanwhile, ductile fracture models that depend on stress triaxiality (η) and Lode angle (θ)
138 were proposed by a number of researchers [24,25,40] and extended to ELCF conditions. Bai
139 [15] and Algarni et al. [16] extended the MMC model [25] which only accounted for
140 monotonic loading, by adopting two weighting functions to account for the nonlinear damage
141 accumulation and the reverse loading effects. Wen and Mahmoud [12,18] developed an
142 analogous nonlinear damage evolution rule to take account of the coupling effects of
143 nonlinearity of material properties caused by load reversal and load history. They also
144 employed this nonlinear damage evolution rule to extend the ductile fracture model [40] to
145 include reverse loading conditions. A phenomenological ductile fracture model incorporating
146 a corresponding nonlinear damage accumulation rule will be adopted in the present study.

147 *2.1. Modified Mohr-Coulomb (MMC) ductile fracture model*

148 Bai and Wierzbicki [25] proposed that the three principle stresses in the Cartesian
149 coordinate system could be transformed into a spherical coordinate system in terms of stress
150 triaxiality (η), Huber-von Mises stress ($\bar{\sigma}$), and Lode angle (θ), as given by Eqs. (1) to (3)
151 respectively, to provide the spatial definition for the modified Mohr-Coulomb fracture model
152 [25]. The relationship between the two coordinate systems is illustrated in Fig. 1.

153 $$\eta = \frac{\sigma_m}{\bar{\sigma}} \tag{1}$$

154 $$\bar{\sigma} = \sqrt{3J_2} \tag{2}$$

155 $$\theta = \frac{1}{3}\arccos\left(\xi\right) = \frac{1}{3}\arccos\left(\frac{27}{2}\frac{J_3}{\bar{\sigma}^3}\right) \tag{3}$$

156 where $\bar{\sigma}$ is the Huber-von Mises stress, σ_m is the mean stress, ξ is the normalized third
157 deviatoric stress invariant and J_2 and J_3 are the second and third deviatoric stress invariants
158 respectively.

159 To efficiently detect the initiation of ductile fracture, the Mohr-Coulomb criterion has
160 been extended to ($\bar{\varepsilon}_f$, η , $\bar{\theta}$) space utilizing a non-quadratic yield function proposed by
161 Hosford [41] and a hardening rule dependent on hydrostatic pressure and Lode angle
162 proposed by Bai and Wierzbicki [25], as given by Eq. (4)

163 $$\bar{\varepsilon}_f = \left\{ \begin{array}{l} \frac{A}{c_2} \times \left[1 - c_\eta(\eta - \eta_0)\right] \\ \times \left[c_\theta^s + \frac{\sqrt{3}}{2-\sqrt{3}}\left(c_\theta^{ax} - c_\theta^s\right)\left(\sec\left(\frac{\bar{\theta}\pi}{6}\right) - 1\right)\right] \\ \times \left[\sqrt{\frac{1+c_1^2}{3}}\cos\left(\frac{\bar{\theta}\pi}{6}\right) + c_1\left(\eta + \frac{1}{3}\sin\left(\frac{\bar{\theta}\pi}{6}\right)\right)\right] \end{array} \right\}^{-\frac{1}{n}} \tag{4}$$

164 where $\bar{\varepsilon}_f$ is the equivalent fracture strain, $\bar{\theta}$ is the normalized Lode angle, calculated as (1-
165 $6\theta/\pi$), η is the stress triaxiality, A and n are the material strain-hardening parameters which
166 can be calibrated from the true stress-strain curve by fitting Hollomon's [42] or Swift's [43]
167 power laws and c_η, η_0, c_θ^{ax} and c_θ^s are fracture parameters to describe both the hydrostatic
168 pressure and Lode angle dependences. c_θ^{ax} is equal to unity for $\bar{\theta} \geq 0$ and equal to c_θ^c for
169 $\bar{\theta} < 0$; c_1 and c_2 are the friction coefficient and the maximum shear strength respectively in
170 the Mohr-Coulomb criterion.

171 A total of eight parameters, A, n, c_η, η_0, c_θ^s, c_θ^c, c_1 and c_2, need to be calibrated.
172 However, when the Huber-von Mises yielding function is employed, i.e. $c_\eta = 0$, $c_\theta^s = c_\theta^c = 1.0$,

the fracture criterion in Eq. (4), determined by eight parameters, can be reduced to a four-parameter (A, n, c_1 and c_2) function [25] as given in Eq. (5).

$$\bar{\varepsilon}_f = \left\{ \frac{A}{c_2} \left[\sqrt{\frac{1+c_1^2}{3}} \cos\left(\frac{\bar{\theta}\pi}{6} \right) + c_1 \left(\eta + \frac{1}{3} \sin\left(\frac{\bar{\theta}\pi}{6} \right) \right) \right] \right\}^{-\frac{1}{n}} \tag{5}$$

According to previous research [14,44], a cut-off region exists in the negative stress triaxiality range, where the value of the fracture strain would go to infinity and therefore ductile fracture could not occur. It is very difficult to determine the cut-off region experimentally due to the significant negative stress triaxiality level. Uniform cut-off regions with different constant negative values have been employed in many ductile fracture models [14,18,40,44]. The concept of friction self-locking was adopted herein to define the cut-off region for the MMC model [25], as shown in Eq. (6). It was postulated by Bai and Wierzbicki [25] that the accumulated damage would remain constant beyond this cut-off region.

$$\sqrt{\frac{1+c_1^2}{3}} \cos\left(\frac{\bar{\theta}\pi}{6} \right) + c_1 \left(\eta + \frac{1}{3} \sin\left(\frac{\bar{\theta}\pi}{6} \right) \right) \le 0 \tag{6}$$

2.2 Nonlinear damage accumulation rule

The MMC model was extended by Bai [15] to include reverse loading conditions by introducing a nonlinear damage evolution rule to account for the effects of nonlinear material damage accumulation and loading history, as expressed in Eqs. (7) and (8) respectively.

$$F_D\left(D_{\mathrm{FI}}\right) = \left(c_g D_{\mathrm{FI}} + \frac{c_g}{e^{c_g} - 1} \right) \tag{7}$$

$$F_H\left(D_{\mathrm{FI}}, \mu_h\right) = \left(1 + c_h D_{\mathrm{FI}}^{\beta_1} \mu_h^{\beta_2} \right)^{k_h} \tag{8}$$

where c_g is the parameter of the extension function for the nonlinear damage rule, c_h, β_1, β_2 and k_h are the parameters of the extension function for load-change effects and μ_h relates to the backstress and current stress tensors to capture the reverse loading effects, as defined in Eq. (9).

195 $$\mu_h = \int_0^{\bar{\varepsilon}^{pl}} \left(1 - \frac{\sigma_{ij} : \alpha_{ij}}{\|\sigma_{ij}\| \cdot \|\alpha_{ij}\|}\right) d\bar{\varepsilon}^{pl} \quad (9)$$

196 where α and σ are the backstress and current stress tensor respectively; $\bar{\varepsilon}^{pl}$ is the equivalent
197 plastic strain.

198 The MMC ductile fracture model coupled with a nonlinear damage accumulation rule
199 have been shown to adequately predict ductile fracture under large plastic strain cycles at the
200 material (coupon)-level for 1045 steel [15] and Inconel 718 [16]. The incremental form is
201 shown in Eq. (10) with an assumption that ductile fracture will initiate at the point when the
202 integral value of dD_{FI} is equal to unity during the loading history.

203 $$dD_{FI} = F_D F_H \frac{d\bar{\varepsilon}^{pl}}{\bar{\varepsilon}_f(\eta, \bar{\theta})} \quad (10)$$

204 # 3. Summary of Existing Experimental Investigations

205 *3.1. Test Specimens, Set-up and Loading Protocols*

206 In total, thirteen brace specimens with CHSs and SHSs from three test programmes
207 [2,3,5] were selected in this study to validate the FE models, which incorporated the MMC
208 ductile fracture model with the damage evolution rule. The specimen label, loading protocol,
209 cross-section shape, manufacturing process, geometry and material properties are described
210 and summarized in Table 1. For the selected specimens, the cross-sectional slenderness,
211 $\lambda_s = D/t$ or B'/t, ranges from 9.3 to 21.6, the global slenderness, $\lambda_G = KL/r$, ranges from
212 41 to 131 and the yield strengths range from 326 to 499 MPa. The labels of the test
213 specimens were kept consistent with each reference [2,3,5] as shown in Table 1.

214 Fig. 2(a) shows the details of a typical test set-up and the arrangement of strain gauges
215 and displacement transducers from the test programme [5]. Fixed-fixed end-conditions were
216 provided by the test rigs in the three test programmes. However, due to different connection

arrangements between the tube ends and the end-plates, as shown in Figs. 2(b) and (c), the effective length factors (K) are assumed in accordance with the actual end conditions for each test programme, when considering the global slenderness ($\lambda_G = KL/r$) in Table 1. The axial and lateral displacements were measured using linear variable displacement transducers (LVDTs) and string potentiometers, respectively. In addition, high strength friction grip (HSFG) bolts were used to maintain the global stiffness of the test rig as shown in Fig. 2(a).

The test specimens were subjected to a quasi-static cyclic loading procedure using a displacement-controlled mechanism, which followed three different loading protocols as illustrated in Fig. 2(d). In the test programmes of Sheehan and Chan [5] and Nip et al. [3], the symmetric displacement loading protocol recommended by the European Convention for Constructional Steelwork (ECCS) [46] was adopted. This loading protocol consists of one cycle at each level of $0.25\Delta_y$, $0.5\Delta_y$, $0.75\Delta_y$ and $1.0\Delta_y$ and three cycles at each level of $2\Delta_y$, $4\Delta_y$, $6\Delta_y$, $8\Delta_y$, etc., where Δ_y represents the estimated axial yield displacement. Two loading protocols for the pipe specimens in Fell's test programme [2] were developed to account for the effects of different types of ground motion, i.e. far-field and tension dominated near-field motions. The second protocol was designed to generate a tension-sensitive failure mode, such as net-section fracture, which is outside the scope of the current investigation. Therefore, the test specimens under the far-field loading protocol were selected to validate the FE models.

3.2. Hysteretic response and failure mode

All test specimens underwent global buckling during the first few cycles of loading after surpassing the yield displacement. After successive inelastic loading cycles, the stiffness near the mid-length region deteriorated, leading to the occurrence of local buckling at mid-length. The numbers of cycles to global buckling and local buckling for each specimen in the three test programmes are summarized in Table 2. The load-displacement hysteresis curves [3,5] are presented in Figs 3 and 4. The shape of the hysteresis curve was significantly influenced

by the global slenderness, KL/r, which also lead to a different energy dissipation capability.

Once local buckling occurred, the localized strains developed rapidly at particular locations in the member, resulting in fracture initiation. For the CHS members, the fracture initiated at the tube face on the concave side after it buckled at the mid-length during the tensile phase of a cycle as shown in Fig. 5. For the SHS members, Figs. 6(a) and (b) indicate that the fracture initiated at the two corners of the locally buckled region and propagated to the flat portion at the mid-length. In addition, fracture in the heat-affected zone adjacent to the stiffeners was observed in some cold-formed (CF) SHS specimens as shown in Fig. 6(c). Though the load-carrying capacity would experience a sudden drop after complete fracture, all test specimens survived for several cycles after local buckling. The numbers of cycles corresponding to the different stages of fracture are presented in Table 2.

4. Numerical Modelling of Local Buckling Induced Fracture

4.1. FE modelling methodology

ABAQUS/Standard [47] finite element software was used to carry out a quasi-static simulation of the bracing members under ELCF loading conditions [46], The hysteretic response, fracture initiation and fracture propagation were recorded in each simulation. Utilizing two lines of symmetry, only one-quarter of the bracing members were modelled, as shown in Fig. 7. The axial load was applied by utilising a displacement boundary condition at the reference point, RP-2. All degrees of freedom of RP-2 were coupled with those at the end of the brace. The same displacement histories as used in each test programme [2,3,5] were implemented in the validation models. The displacement history type "C" [3] as shown in Fig. 2(d) was adopted in the parametric investigation, which followed the loading protocol recommended by ECCS [46] and began with tensile force at each cycle.

The three-dimensional solid element, C3D8R [48], was adopted in the FE models. FE models using shell elements, S4R [48], were also constructed for comparison. Shell elements

can simulate the buckling and post-buckling performance of tubular structures with relatively low computational time and high accuracy in comparison with solid elements. The full hysteretic responses and the key points of the fracture process, i.e. cracking initiation and full fracture are compared with the experimental results in Fig. 8. A moderate difference was found in the tensile strengths. The solid elements were found to be more suitable for simulating the ELCF fracture process than the shell elements, as they could simulate the whole crack propagation process as defined in Fig. 9. Nevertheless, the choice of element did not influence the cycle in which the prediction of fracture occurred. Therefore C3D8R-element based models were adopted in this investigation.

A refined mesh was used in the regions of the mid-length and the end of the models, where local buckling was anticipated to occur. The length of the refined regions is presented in Fig. 7. Mesh sensitivity and convergence studies were conducted for element sizes of 1 mm, 1.5 mm and 3.0 mm for the refined region in both the longitudinal axis and the circumferential directions; an element size of 15 mm was used for the coarse mesh region. The number of elements through the thickness was set as the larger of three and $t/1.5$. It was found that the 3 mm coarse mesh significantly postponed the occurrence of cracking through the tube-wall, although there was only a minor effect on the fracture initiation, as presented in Fig. 10. Considering the computational time, an element size of 1.5 mm was adopted in the subsequent FE analyses. The total number of elements for a specimen with a diameter of 48 mm and a length of 1500 mm was approximately 38,000. A typical mesh is presented in Fig. 7.

Geometric imperfections, including both initial global and local imperfections, were introduced in the FE models based on the superposition of weighted eigenmode analysis data. A sensitivity study was conducted to assess the influence of the initial imperfections on buckling and fracture. The amplitudes of global and local imperfections ranged from $L/500$ to $L/5000$ and $t/50$ to $t/500$, respectively. Global buckling occurred at an earlier stage for models

with larger imperfection amplitudes, while the occurrence of fracture initiation differed by one cycle among the investigated ranges. Following comparisons between the numbers of cycles to global buckling, local buckling and fracture, the optimum imperfection amplitudes for each test programme and parametric study are listed in Table 2. The same imperfection values as those measured for the CHS bracing members in [5] i.e. $L/2000$ for the global imperfection and $t/100$ and $t/150$ respectively for the local imperfection in the cold-formed and hot-rolled members, were used in the parametric studies.

4.2. Plasticity and fracture models

4.2.1 Plasticity modelling

In order to reliably predict ELCF fracture, accurate simulations are needed of the stress-strain evolution under cyclic loading. A constitutive model using the Huber-von Mises yield criterion and a combined isotropic/kinematic hardening rule in ABAQUS [48] was adopted, which was based on the work by Lemaitre and Chaboche [49]. This model took the Bauschinger effect under cyclic loading into consideration. The evolution law consisted of a nonlinear kinematic hardening component using the backstress, α, as described in Eq. (11) and an isotropic hardening component as a function of equivalent plastic strain as given in Eq. (12).

$$\alpha = \sum_{k=1}^{n} \alpha_{\mathrm{k}} \; ; \qquad d\alpha_k = C_k \frac{1}{\sigma_0}\left(\sigma - \alpha\right) d\bar{\varepsilon}^{pl} - \gamma_k \alpha_k d\bar{\varepsilon}^{pl} \tag{11}$$

where σ_0 is the size of the yield surface defined in Eq. (12), $\bar{\varepsilon}^{pl}$ is the equivalent plastic strain, C_{k} is the k^{th} initial kinematic hardening modulus, γ_{k} is the k^{th} rate of decrease of C_{k}, α is the overall backstress and α_{k} is the k^{th} backstress;

$$\sigma_0 = \sigma\big|_0 + Q_\infty\left(1 - e^{-b\,\bar{\varepsilon}^{\mathrm{pl}}}\right) \tag{12}$$

where $\sigma|_0$ is the yield stress at zero plastic strain, Q_∞ is the maximum change in size of yield surface, *b* is the rate of change of yield surface size with increasing plastic strain.

The hardening effect was considered over a region including the corner and an extension along the flat face of the tube equal in length to the tube thickness. The model parameters of the combined isotropic/kinematic hardening rule were calibrated according to the ABAQUS documentation [48] for each test programme, as listed in Table 3.

4.2.2 Fracture modelling

The framework of continuum damage mechanics [49] is adopted in this research to describe the material behaviour with due consideration of progressive damage degradation as adopted in ABAQUS [48]. A typical uniaxial stress-strain curve with progressive damage degradation is shown in Fig. 11 (solid curve *a*-*b*-*c*-*d*). The curve *a*-*b*-*c*-*d*' represents the behaviour of the material without considering the damage. Point c marks the onset of damage (taken as fracture initiation). Beyond this point, the material response degrades under the principle of strain-equivalence. In FE simulations performed using ABAQUS, Point *c* is determined from a fracture initiation criterion and the material softening is described using a damage evolution rule.

Ductile fracture of metals is dependent on stress triaxiality (η) and Lode angle (θ). The MMC model [25], proposed and validated at the material level (coupon) in [25] has been adopted in FE models at member-level by Xu et al. [50-52]. This fracture model, incorporating a linear damage accumulation rule, has been used to successfully predict ductile fracture initiation and propagation under monotonic loading. In the current study, the MMC model with a nonlinear damage evolution rule [15,53] was adopted for reverse or cyclic loading conditions.

The MMC fracture model in ($\bar{\varepsilon}_f$, η ,$\bar{\theta}$) space used in conjunction with the Huber-von Mises yield criterion is summarized by Eq. (5) with a corresponding cut-off region described

by Eq. (6). Ideally, a comprehensive material test programme covering tension, compression and shear should be carried out on specially designed coupon specimens to ensure that the stress states of fracture initiation are covered for different stress triaxiality levels. From the results of conventional tensile coupon tests listed in Table 4, the parameters A and n representing the flow strength parameters of the material can be derived. The other parameters, c_1 and c_2, should be calibrated using notched round bars with different notched radii at high stress triaxiality levels and flat specimens (dog-bone, central hole and butterfly types, and circular punch disks) at intermediate and low stress triaxiality levels. The parameters can be determined by minimizing the average equivalent plastic strain error (the difference between test and simulation results) at the onset of fracture. With limited material test data available, a simplified MMC model calibration procedure, using the conventional tensile coupon test results only, was proposed and verified in previous member-level simulations [50-51]. In addition to the parameters A and n, the material parameter c_2 accounting for the shear strength, based on the physical implications of the Mohr-Coulomb model, can be estimated from conventional tensile test results [50]. The friction coefficient parameter c_1 cannot easily be obtained from tensile coupon tests, but can be assumed to be a constant value for materials with similar crystallographic structures. A sensitivity study [50] to assess the effect of this assumption on the prediction of fracture initiation, found that a value of c_1=0.12 is suitable for structural steel with nominal yield strengths ranging from 235 MPa to 345 MPa. The above simplified methodology for the calibration of the model parameters is described in more detail by Xu et al. [50]. The calibrated parameters of the MMC model for each test programme are listed in Table 4.

Under monotonic loading conditions, the linear damage accumulation rule was found to adequately predict material fracture initiation [24,40,54]. However, for the periodic loading cases, the load history effect and the nonlinear damage evolution should be taken into consideration [14-18]. The individual and combined effects on fracture prediction under

366 reverse loading were investigated [18] for steel and aluminium. It was reported that
367 combining the effects of both the loading history and the nonlinear damage evolution
368 provided the most satisfactory correlation. In addition to this, it was found that the sensitivity
369 to the nonlinear intrinsic properties and the load history effect varied with the metal type,
370 among which steel exhibited a strong load history dependence. Therefore, two weighting
371 functions [15] with respect to nonlinear accumulation (in Eq. (7)) and the load history effect
372 (in Eq. (8)) were adopted in this study. The damage evolution rule employed is presented in
373 Eq. (10) in an incremental form, where dD_{FI} is the damage increment, $\bar{\varepsilon}^{pl}$ is the equivalent
374 plastic strain, as shown in Eq. (13), and $d\bar{\varepsilon}^{pl}$ is the equivalent plastic strain rate.

375 $$\bar{\varepsilon}^{pl} = \int_0^t \sqrt{\frac{2}{3} d\varepsilon^{pl} : d\varepsilon^{pl}}\, dt \tag{13}$$

376 The range of the damage indicator, D_{FI}, is assumed to be [0,1.0], if the material of the
377 structural members is assumed to be without initial cracks or accumulated plastic strains, and
378 the effect of the hardening history from the manufacturing process on the damage
379 accumulation is not considered. D_{FI} = 0 represents the material behaviour before the plastic
380 stage, while D_{FI} = 1.0 indicates the fracture initiation. The parameters, c_g for nonlinear
381 accumulation and c_h, β_1, β_2 and k_h, for the load reversal effect should be calibrated by material
382 test results under reversed or cyclic loading and replicated in the numerical simulations on the
383 basis of the minimum error criteria of the fracture equivalent plastic strain as used in the
384 MMC model calibration. Due to lack of essential data for each test programme, a sensitivity
385 study was conducted herein based on the available experimental data for steel 1045 from [15].
386 It was found that k_h, representing load history effects, had the most significant effect on
387 fracture initiation in comparison with the other five parameters. The greatest difference in the
388 cycle of occurrence of fracture was more than six cycles when k_h ranged from -0.6 to 1.0, as
389 shown in Fig 12. Therefore, a calibration process based on the bracing member tests was used
390 to obtain an optimal group of these parameters. The group of parameters sought would

minimize the average errors for the number of cycles to fracture between the experimental and numerical results. The resulting group of consistent values of c_g, c_h, β_1, β_2 and k_h is listed in Table 4. For the test specimen HF-H-1500, the evolution of the accumulation damage indicator, D_{FI}, with the stress triaxiality and normalized Lode angle during periodic loading are shown in Figs. 13(a) and (b), respectively. An interesting phenomenon was also observed that the normalized Lode angle was more sensitive than the stress triaxiality in manifesting the stage alterations, such as local buckling and fracture initiation.

A post-initiation softening rule was also employed by using a linear relationship between the material degradation and the equivalent plastic strain. To avoid significant dependence on the mesh, the effective plastic displacement was used instead of the equivalent plastic strain [48], as shown in Eqs. (14a), (14b) and (15). The introduction of the post-initiation softening rule can help to simulate the fracture propagation and correct crack modes [16,55,56] and achieve better convergence without a sudden degradation of stress for an element when using the implicit calculation technique. As illustrated, the softening rule is defined in terms of effective plastic displacement by using the characteristic length to alleviate the mesh dependence [48] as shown in Eq. (15).

$$\widetilde{E} = E\,(1\text{-}D_{\text{post}}) \tag{14a}$$

$$\tilde{\boldsymbol{\sigma}} = \boldsymbol{\sigma}/\,(1\text{-}D_{\text{post}}) \tag{14b}$$

where $\widetilde{E}$ is the elastic modulus of the damaged material, E is the elastic modulus of the material free of damage, $\tilde{\boldsymbol{\sigma}}$ is the effective stress tensor, $\boldsymbol{\sigma}$ is the usual stress tensor, and D_{post} is the damage variable.

$$dD_{\text{post}} = \frac{L_C d\bar{\varepsilon}^{pl}}{\bar{u}_f^{pl}} \tag{15}$$

where L_C is the characteristic length of the element for a specified FE model.

The MMC model with the nonlinear damage accumulation rule was incorporated into the FE models using a user subroutine, USDFLD. The option of element deletion control is

not offered in ABAQUS/Standard when using USDFLD. Therefore, an element was set to fail at a maximum post-initiation degradation with a residual stiffness of 2% to avoid severe non-symmetry of the Jacobian matrix and convergence problems. The flow chart for the USDFLD of the ELCF fracture model is presented in Fig. 14.

4.3. Validation

Test specimens from three different test programmes [2,3,5] for both CHS and SHS bracing members were replicated by the FE models. The experimental and numerical results were compared with respect to the number of cycles to buckling, hysteretic response, and fracture process, including initiation and propagation. The models simulated local buckling induced ductile fracture under ELCF loading to a satisfactory degree of accuracy.

The force-displacement curves from the experimental and numerical results, as shown in Figs. 3 and 4, were in a good agreement. The primary points of the fracture processes, i.e., initiation, corner opening and full fracture, are also shown and compared between the test (if they were available) and simulation results in Figs. 3 and 4. In addition, the numbers of cycles to global buckling, local buckling and fracture are compared in Table 2. The definitions of the different stages for ELCF fracture are presented in Fig. 9. Generally, the results were reasonably accurate, though in certain simulations, the FE models failed to undergo the complete loading history due to convergence problems after the initiation of fracture. This is because material models exhibiting softening behaviour and stiffness degradation often lead to severe convergence difficulties in implicit analysis programmes [48], though some pre-cautions to avoid convergence problems were taken in the FE models.

The comparisons of the ELCF fracture failure mode and its evolution for the CHS and SHS bracing members are given in Figs. 5 and 6 respectively. The regions marked in red were at the maximum degradation value of D_{post}, which indicated crack propagation. Different failure modes and fracture locations observed in the tests, i.e., fracture due to local

buckling at the mid-length (Figs. 5 and 6(a, b)) and fracture near stiffeners (in Fig. 6(c)), were accurately predicted by the numerical simulations. Despite this, it should be noted that once a visual crack formed, the existence of the sharp crack tip required a more refined mesh near the cracking region to capture the crack propagation precisely. Furthermore, in order to accurately simulate the fracture process on a micro-scale, a fracture model would need to be developed that could capture the various fracture mechanisms depending on the stress intensity, stress triaxiality and Lode angle.

5. Parametric Analyses and Proposed Prediction Formulations

The slenderness parameters (normalized global and local slenderness) in the parametric study were chosen based on the validated FE models. Tables 4 and 5 present the material properties and specimen matrix in the parametric study respectively. The effect of the manufacturing process was considered using the calibrated material parameters from hot-rolled and cold-formed tubes [57]. The loading protocol "Type C" illustrated in Fig. 2(d) was adopted.

5.1. Deformation capacity and localized strain prior to fracture

In the experimental investigations [1-7], the localized strain accumulated dramatically through successive cycles after the occurrence of local buckling. Figs. 15 and 16 present the typical deformed-shape of the brace at the maximum compressive displacement prior to local buckling and fracture, with the yielded regions clearly indicated, as observed in the parametric study. A plastic hinge approach considering the evolution of global and local strains [58] was adopted and improved to develop a prediction model of localized strain prior to ELCF fracture.

5.1.1 Global hinge angle, global plastic hinge length and global buckling induced strain, θ_1, L_{H_G} and ε_G

Fig. 15(a) shows that the plastic hinges formed at the middle and two ends of the brace during global buckling. The length between the two end-hinges, denoted L_H, was employed instead of member length, L, in the plastic hinge model. Therefore, based on the simplified model, the average strain due to global buckling at the maximum compressive displacement prior to local buckling can be expressed as follows:

$$\varepsilon_G = \frac{D\,\theta_1}{L_{H_G}} \tag{16}$$

where D is the outer diameter of the CHS brace, L_{H_G} is the global hinge length developed at the mid-length of the brace as shown in Fig. 15(b) and θ_1 is the global hinge angle. The global hinge length can be determined [2] from Eq. (17)

$$L_{H_G} = \frac{\int_0^{L_{Y_G}} \varphi(x)\,\mathrm{dx}}{\varphi_{max}} \tag{17}$$

where L_{Y_G} is the length of the yielded region at the mid-length, $\varphi(x)$ is the curvature within this region and φ_{max} is the maximum curvature value.

From the geometrical relationship of the deformed brace, θ_1 can be calculated as follows:

$$\theta_1 = \arcsin\left(2\Delta_1 / L_H\right) \tag{18}$$

where Δ_1 is the out-of-plane deformation amplitude shown in Fig. 15(a).

It should be noted that L_H is different from the effective length, KL, defined earlier. The location of the end-hinges can be approximately defined as the points of the maximum curvature within the yielded region at the two ends. From the parametric study, L_H is approximately equal to $0.968(L\text{-}2L_P)$, where L_P is the stiffener length at both ends of the bracing member.

The parameters θ_1 and L_{H_G} indicate the deformation capacity of a bracing member prior to local buckling. They depend on the inherent material properties and geometry of braces. A parametric study was conducted to derive the values of θ_1 and L_{H_G}. They were evaluated

based on Eqs. (17) and (18) from the numerical results. Two normalized global and cross-sectional slendernesses, $\overline{\lambda}_{\mathrm{G}}$ and $\overline{\lambda}_{\mathrm{S}}$, were introduced to account for the material and geometry effects and to accommodate the design approach of AISC 341-10 [36], as shown in Eqs. (19) and (20) respectively.

$$\overline{\lambda}_{G} = \frac{KL/r}{\lambda_{\mathrm{limit}}} \tag{19}$$

$$\overline{\lambda}_{\mathrm{S}} = \frac{D/t}{\lambda_{\mathrm{hd}}} \tag{20}$$

where K is the effective length factor, taken equal to 0.5 for the fixed-ended conditions employed in the parametric study, L is the brace length, r is the radius of gyration of the brace, λ_{limit} is the brace slenderness limit in an ordinary concentrically V or inverted-V braced frame in AISC 341-10 [36], $\lambda_{\mathrm{limit}} = 4\sqrt{E/f_{\mathrm{y}}}$, t is the tube-wall thickness, λ_{hd} is the limit of the width-to-thickness ratio for highly-ductile members in AISC 341-10, $\lambda_{\mathrm{hd}} = 0.038\,E/f_{\mathrm{y}}$ and E and f_{y} are elastic modulus and yield strength of the material.

The relationship between global hinge angle θ_1 and global plastic hinge length $L_{\mathrm{H_G}}$ with the two normalized parameters $\overline{\lambda}_{\mathrm{G}}$ and $\overline{\lambda}_{\mathrm{S}}$ are presented in Figs. 17 and 18, respectively. As indicated in Figs 17(a) and (b), the hot-rolled (HR) braces experienced slightly higher deformations before local buckling than their cold-formed (CF) counterparts, especially when the members did not exceed the limits of highly-ductile members, $D/t = 0.038E/fy$ in AISC 341-10 [36]. However, as shown in Figs. 18(a) and (b), little discrepancy was found regarding the plastic hinge length $L_{\mathrm{H_G}}$. When the values of KL/r and D/t are set at 50 and 18 respectively, below the limits in AISC 341-10, the influence of the two normalized parameters on the tube deformation θ_1 and plastic strain accumulation level $L_{\mathrm{H_G}}$, along with their defining equations, are presented in Figs. 17 and 18, respectively. The bracing members

with stocky cross-sections and large slendernesses would have a larger value of θ_1 but a smaller value of (L_{H_G}/L_H) compared to the others. This indicates that these braces will experience more cycles before the occurrence of local buckling, as observed in the experimental investigations [3,5].

Expressions for the global hinge angle and plastic hinge length, θ_1 and L_{H_G} are proposed in Eqs. (21) and (22) respectively. The comparisons between the numerical and calculated values for θ_1 and L_{H_G} are shown in Figs 17(c) and 18(c) respectively. By substituting Eqs. (21) and (22) into Eq. (16), the average strain developed in the mid-length region before local buckling can be quantified.

$$\theta_1 = A_{\theta 1}\,\overline{\lambda}_S^{\,B_{\theta 1}}\,\overline{\lambda}_G^{\,C_{\theta 1}} \tag{21}$$

$$\begin{aligned} L_{H_G} &= \left(A_{H_G}\,\overline{\lambda}_S^{\,B_{H_G}}\,\overline{\lambda}_G^{\,C_{H_G}}\right) L_H \\ &= 0.968\left(A_{H_G}\,\overline{\lambda}_S^{\,B_{H_G}}\,\overline{\lambda}_G^{\,C_{H_G}}\right)(L - L_P) \end{aligned} \tag{22}$$

where $A_{\theta 1}$, $B_{\theta 1}$ and $C_{\theta 1}$ are parameters for θ_1 listed in Table 6 and A_{H_G} and B_{H_G} are parameters for L_{H_G} listed in Table 6.

5.1.2 Local hinge angle, local plastic hinge length and local buckling induced strain, θ_2, L_{H_L} and ε_L

After the occurrence of local buckling, localized strains accumulate at the peak of the buckling wave. The local plastic hinge length L_{H_L} was determined in the same way as the global plastic hinge length L_{H_G}, as shown in Fig. 15(b), with reference to the FE results. The deformed shape of the local buckling was assumed to be a sinusoidal function [59], given as $-A\sin\left(\frac{m\pi x}{L}\right)$, where A and m are functional constants and L is the brace length. It was found that local buckling developed symmetrically at the mid-length of all braces. Therefore,

531 the simplified representation of the brace at the maximum compressive displacement prior to
532 fracture shown in Fig. 16 was adopted.

533 It was assumed that a local plastic hinge (i.e., through the thickness of tube wall)
534 occurred at each end and one at the mid-length on the compressive tube-wall, as marked in
535 Fig. 16(a). The analytical model for the local bucking at mid-length is shown in Fig. 16(b).
536 This model assumed that only localized strain caused by local buckling was accumulated in
537 the tube-wall after local buckling. The length of the local buckling region $L_{\text{half_w}}$ was
538 determined based on the actual buckling-half-wave derived from the numerical results.

539 In a similar manner to the derivation of the average strain for global buckling ε_{G} at the
540 member mid-length, the average localized strain for local buckling ε_{L} can be approximated
541 by Eq. (23) when taking the locally deformed tube-wall as a tube with a diameter of t.

542 $$\varepsilon_{\text{L}} = \frac{t\,\theta_2}{L_{\text{H_L}}} \tag{23}$$

543 where t is the tube-wall thickness, θ_2 is the local hinge angle as shown in Fig. 16(b) and $L_{\text{H_L}}$
544 is the local plastic hinge length.

545 According to the definition of $L_{\text{H_G}}$ and θ_1, the local hinge length $L_{\text{H_L}}$ and local hinge
546 angle θ_2 can be derived from Eqs. (24) and (25), based on the analytical model in Fig. 16(b).

547 $$L_{\text{H_L}} = \frac{\int_0^{L_{\text{Hafl_W}}} \varphi(x)\,\text{dx}}{\varphi_{\max}} \tag{24}$$

548 $$\theta_2 = \sin^{-1}\left(2\Delta_2 / L_{\text{Half_W}}\right) \tag{25}$$

549 where $L_{\text{Half_W}}$ is the local buckling half-wave length, $\varphi(x)$ and $\varphi_{\max}$ are the curvature
550 function of a half-wave and its maximum value respectively. Δ_2 is the deformation amplitude
551 as shown in Fig. 16(b).

552 The parameters of θ_2 and $L_{\text{H_L}}$ manifest the local deformation capacity and plastic strain

553 level of a brace member prior to fracture. From the parametric study, the local hinge angle θ_2
554 can be expressed as in Eq. (26).

555 $$\theta_2 = A_{\theta 2}\left(\left(\overline{\lambda}_S - 1\right)^2 + B_{\theta 2}\right)\left(\overline{\lambda}_G + C_{\theta 2}\right) \quad (26)$$

556 where $A_{\theta 2}$, $B_{\theta 2}$ and $C_{\theta 2}$ are parameters for θ_2 listed in Table 6.

557 As shown in Fig. 19(a), the hot-rolled (HR) braces exhibited clearly superior local
558 deformation capacity with higher values of θ_2 at the onset of fracture than the CF braces. The
559 value of θ_2 varied for a stocky cross-section member ($D/t < \lambda_{hd}$) while the value dropped when
560 D/t exceeded λ_{hd}, especially for the CF members. As shown in Fig. 19(b), the variation with
561 the normalized member slenderness was approximately linear, and it indicated that a slender
562 bracing member would experience less severe local buckling deformation than a stocky
563 member before fracture. Fig. 19(c) shows good correlation between the θ_2 values obtained
564 from the FE models using Eq. (25) and the values calculated from the proposed Eq. (26).

565 The local plastic hinge length was found to have a linear relationship with the
566 theoretical wave-length of symmetrical local buckling for a cylindrical shell under uniform
567 axial compression [59]. It was assumed that buckling occurred at a stress within the
568 proportional limit. The half-wave length from Timoshenko's elastic stability theory is
569 calculated as Eq. (27).

570 $$L_{Half_W}^{Elastic} = \pi \sqrt[4]{\frac{D^2 t^2}{48\left(1-\upsilon^2\right)}} \quad (27)$$

571 where v is Poisson's ratio, taken equal to 0.3.

572 Though Timoshenko also proposed an equation for local buckling deflection, $w(x)$ [59],
573 it was based on elastic buckling and a uniform compression loading which was quite different
574 from the local buckling of the bracing members. The brace buckled beyond the proportional
575 limit and this buckling was combined with flexural buckling. Therefore, the theoretically
576 proposed elastic deflection function could not be used to calculate the curvature. In this study,

577 the local hinge length L_{H_L} was calculated from the simulation results using Eq. (24). The
578 relationship between $L_{Half_W}^{Elastic}$ and L_{H_L}, expressed in Eq. (28), is shown in Fig. 20. A longer
579 local hinge length could be developed prior to fracture for the HR bracing members.

580
$$\begin{aligned} L_{H_L} &= A_{H_L} L_{Half_W}^{Elastic} + B_{H_L} \\ &\approx 1.22 A_{H_L} \sqrt{Dt} + B_{H_L} \end{aligned} \tag{28}$$

581 where A_{H_L} and B_{H_L} are parameters for L_{H_L} listed in Table 6.

582 Substituting Eqs. (26) and (28) into Eq. (23), the average localized strain that
583 developed at the member mid-length at the maximum compressive displacement prior to
584 fracture can be quantified.

585 5.1.3 Localized strain induced by coupling effects of global and local buckling

586 The localized strain at the maximum compressive displacement prior to fracture ε_F,
587 consists of global and local buckling induced strains, namely ε_G and ε_L, and an expression for
588 this is proposed in Eq. (29).

589
$$\varepsilon_F = \frac{D\theta_1}{L_{H_G}} + \frac{t\theta_2}{L_{H_L}} \tag{29}$$

590 For a given a brace member with a specified material property and manufacturing process,
591 the critical localized strain due to cyclic loading prior to fracture given by Eq. (29) can be
592 calculated by substituting Eqs (21), (22), (26) and (28). It is reported in the previous studies
593 [9,60] that the 45°-region of the compressive section would accumulate a high-level of plastic
594 strain. Therefore, the average values of equivalent Mises strain, $\varepsilon_{F_FEA} = \sqrt{\frac{2}{3}\varepsilon_{ij} : \varepsilon_{ij}}$, obtained
595 from the numerical results in the 45°-region of the compressive side at the mid-length were
596 compared with the prediction values calculated using Eq. (29) in Fig. 21. The mean values of
597 the calculation-to-FE results were 1.00 and 1.03 for the HR and CF braces respectively,

598 demonstrating that the developed localized strain prediction model had a satisfactory degree
599 of accuracy. Furthermore, the proposed equation for the localized strain prior to fracture can
600 be used in fiber-based FE models of the bracing members in a structural analysis to capture
601 buckling induced fracture failure.

602 *5.2. Fracture life*

603 5.2.1 Global hinge rotation at maximum compressive displacement before fracture θ_3

604 Empirical models have previously been proposed to predict the fracture life of hollow
605 structural section bracing members and these have generally been expressed in terms of
606 indices of displacement ductility (μ_Δ) [2] and rotation ductility [61]. It is more desirable to
607 have prediction models that are associated with the material and geometry properties instead
608 of depending on the loading history, since these can easily be used by design engineers
609 without knowing the displacement history in advance. Tremblay et al. [61] identified the
610 discrepancy of prediction accuracy between the two bracing systems, i.e. single bracing and
611 X-bracing members, when applying an equation in terms of displacement index (μ_Δ).
612 Therefore, the rotation in the global plastic hinge prior to fracture was used to predict the
613 fracture life of SHS bracing members [61]. In addition, some established prediction models
614 derived from experimental and numerical fracture life data of cold-formed and hot-rolled
615 members did not consider the effect of the manufacturing process on the fracture life.
616 However, the differences in the ductility capacity between cold-formed and hot-rolled braces
617 with the same geometry were observed in the previous tests [3,7]. The rotation index was
618 therefore adopted to assess the fracture life of CHS bracing members with different
619 manufacturing processes.

620 The plastic hinge model and the relationship between axial shortening displacement Δ_C
621 and rotation θ_3 at the maximum compressive displacement prior to fracture, are presented in
622 Fig. 22(a). It is assumed that the axial shortening (Δ_C) is only contributed to by the brace

623 rotation at the mid-length hinge of an uncompressible brace. The relationship between Δ_C and
624 θ_3 is expressed in Eq. (30), and when the approximation of $\sin(\theta_3) \approx \theta_3$ is adopted, Eq. (30)
625 can be mathematically simplified to Eq. (31) which coincides with the equation used by
626 Tremblay et al. [61] for single bracing members.

627 $$\Delta_C = L_H(1-\cos\theta_3) \tag{30}$$

628 $$\Delta_C = \frac{L_H}{2}\theta_3^2 \tag{31}$$

629 where θ_3 is the maximum global hinge angle before fracture, defined in Fig. 16(a) and Δ_C is
630 the maximum compressive displacement before fracture, which includes both permanent
631 plastic tensile displacement and compressive displacement, illustrated in Fig. 22 (a).

632 A parametric study was conducted to estimate the influence of the normalized
633 parameters $\overline{\lambda}_G$ and $\overline{\lambda}_S$ on the fracture life index θ_3. The values of θ_3 were calculated by Eq.
634 (32) without assuming the approximation of $\sin(\theta_3) \approx \theta_3$, since θ_3 was no longer a small
635 value (≥ 10°).

636 $$\theta_3 = \sin^{-1}(2\Delta_3 / L_H) \tag{32}$$

637 The variation of θ_3 with $\overline{\lambda}_G$ and $\overline{\lambda}_S$ is illustrated in Figs. 23(a) and (b) respectively. A
638 similar relationship with the two buckling parameters was found for θ_1 (Fig. 17) and θ_3 (Fig.
639 23).

640 $$\theta_3 = A_{\theta 3}\,\overline{\lambda}_S^{\,B_{\theta 3}}\,\overline{\lambda}_G^{\,C_{\theta 3}} \tag{33}$$

641 where $A_{\theta 3}$, $B_{\theta 3}$ and $C_{\theta 3}$ are parameters for θ_3 listed in Table 6.

642 As anticipated, the rotation at the maximum compressive displacement prior to fracture
643 θ_3 decreases with $\overline{\lambda}_S$ and increases with $\overline{\lambda}_G$, exhibiting the same variation tendency as the
644 maximum rotation θ_1 before local buckling. However, the discrepancy in deformation
645 capacity between cold-formed and hot-rolled bracing members is more significant, especially

646 when the ratio of diameter to thickness is below the limit of highly-ductile members in AISC
647 341-10 [36], as shown in Fig. 23(a). Fig. 23(c) demonstrates that the proposed equation, Eq.
648 (33) can reliably predict the global rotation prior to fracture θ_3.

649 5.2.2 Relationship between θ_3 and displacement ductility μ_c.

650 Based the analytical plastic hinge model shown in Fig. 22 (a), Δ_C can be taken to be
651 equal to $\Delta_Y(\mu_c+\mu_t-1)$, where μ_c and μ_t are the anticipated compressive and tensile ductilities,
652 respectively. For a specified bracing member under a symmetric cyclic loading history ($\mu_c =$
653 μ_t), the elastic displacement is equal to Lf_y/E. Therefore, Δ_C can be expressed as follows,

654 $$\Delta_C = L\left(2\mu_c - 1\right)\left(f_y / E\right) \tag{34}$$

655 Combining Eq. (30) with Eq. (34), μ_c can be expressed in terms of θ_3 in Eq. (35), where L_H is
656 approximately equal to $0.968L$, based on the previous parametric study. It should be noted
657 that the relationship between L_H and brace length L may vary for different end boundary
658 conditions.

659 $$\begin{aligned}\mu_c &= \frac{1-\cos\theta_3}{f_y / E}\frac{L_H}{2L}+\frac{1}{2}\\ &= 0.484\left(1-\cos\theta_3\right)\frac{E}{f_y}+\frac{1}{2}\end{aligned} \tag{35}$$

660 where μ_c is the displacement ductility, θ_3 is the maximum global rotation, calculated by Eq.
661 (33) and E and f_y are the elastic modulus and yield strength of the material respectively.

662 Therefore, the prediction model for θ_3 can be used to demonstrate the maximum ductility
663 μ_{max} that can be achieved for a given bracing member. The maximum allowable ductility
664 level for bracing members at the global slenderness limit and sectional slenderness limits
665 specified in AISC 341-10 can be derived from Figs. 24 (a) and (b) respectively. Hot-rolled
666 CHS bracing members exhibit superior ductility to cold-formed braces, which can be
667 achieved when the limit of $D/t = 0.038E/f_y$ for highly-ductile members proposed in AISC
668 341-10 [36] is not exceeded. Significant discrepancies are only observed between HR and CF

members when the normalized parameter $\overline{\lambda}_S$ (= $(D/t)/\lambda_{hd}$) is equal to or below the value of 1.0, as indicated in Figs. 24(a) and (b).

6. Discussions

Fig. 22(b) shows the relationship between story drift angle θ_s and the brace deformation, Δ, in a one-story chevron braced frame [2]. Based on this, the relationship between the axial deformation range of the brace Δ_{range} and the maximum story drift angle θ_{s_max} (expressed in radians) was proposed by Fell [2] in Eq. (36)

$$\theta_{s_max} = \frac{\Delta_{range} / L_B}{(1+\alpha_s)(1+C)\cos\beta_s \sin\beta_s} \tag{36}$$

where α_s is the ratio of maximum to minimum drift angle demands within one story, which is equal to 0.4 as proposed by Fell [2], C is the ratio of the rigid-link length (on both ends of the brace) to L_B, equal to zero for simplification, L_B is the brace length, β_s is brace angle and Δ_{range} is the axial deformation range equal to $\Delta_C + \Delta_Y$.

Based on the definition shown in Fig 22(a), the brace axial deformation range $\Delta_{range} = \Delta_C + \Delta_Y$ can be used in conjunction with Eq. (34) with the assumption that only the length between the two end-hinges L_H is considered, i.e., setting L_B equal to L_H. Therefore, the maximum drift demand θ_{s_max} for a one-story chevron braced frame (brace angle of 45°) can be expressed in terms of maximum rotation before fracture θ_3 in Eq. (37).

$$\theta_{s_max} = \frac{10}{7}\left(\frac{f_y}{E} + 1 - \cos\theta_3\right) \tag{37}$$

The dependence of θ_{s_max} on the normalized cross-sectional slenderness $\overline{\lambda}_S$ (in Fig. 25(a)) and normalized global member slenderness $\overline{\lambda}_G$ (in Fig. 25(b)) is illustrated in Fig. 25. Values of $\overline{\lambda}_S$ and $\overline{\lambda}_G$ less than unity imply a highly-ductile configuration within the slenderness limit in AISC 341-10 [36]. The maximum story drift angle (θ_{s_max}) has the same

691 variation tendency with the two buckling parameters as the displacement ductility (μ_c). There
692 is an interesting observation in Fig. 25(a), for a bracing member at the highly-ductile section
693 limit (i.e., $\overline{\lambda}_S = 1.0$) and global slenderness of $0.7\lambda_{limit}$, the calculated maximum story drift
694 angle θ_{s_max} is slightly less than 0.04 rad, which is the requirement for highly-ductile
695 members in AISC 341-10 [36] and also is defined as the "maximum considered earthquake"
696 demand [2,62]. As anticipated, the story drift angle capacity of the cold-formed bracing
697 member is much lower when compared with the hot-rolled one. As shown in Fig. 25(a), only
698 when the value of D/t is less than $0.835\lambda_{hd}$ will the capacity be attained. However, this
699 superior cross-sectional performance of hot-rolled members in comparison with the cold-
700 formed counterparts can only be guaranteed for those sections with the sectional slenderness
701 not exceeding λ_{hd}. In the 2016 seismic design provisions (AISC 341-16 [62]), the limit value
702 of sectional slenderness for the highly-ductile member, λ_{hd}, became $0.053(E/R_y f_y)$ instead of
703 $0.038(E/f_y)$ in the 2010 version [36].

704 In Fig. 25(b) it is also found that the bracing members with a small global slenderness
705 (less than $0.726\lambda_{limit} \approx 2.9\sqrt{E/f_y}$) cannot meet the 0.04 rad story drift angle, even though
706 they possess a stocky cross-section that satisfies the slenderness limit of λ_{hd}. This can be
707 attributed to the severe local buckling that may cause premature fracture for these less slender
708 bracing members.

709 In the AISC seismic provisions [36,62], the member and sectional slenderness are
710 determined separately. However, from the experimental observations [1-7], the combined
711 effect of global and local bucking should be considered in the assessment of the fracture life
712 of a bracing member. In this investigation, the analytically proposed equations, i.e., Eqs. (33),
713 (35) and (37) explicitly demonstrate that the fracture life and ductility of bracing members
714 and the deformation capacity of the braced frame are generally governed by slenderness
715 parameters, including member and sectional slendernesses, and material properties for a

716 specified loading history. Therefore, the interaction of global and local buckling and the
717 effect of this on the deformation capacity is considered, in terms of slenderness parameters, in
718 the proposed equations.

719 It should be noted that the plastic hinge model is developed on the condition of inelastic
720 buckling. Therefore, the proposed model may not be suitable for members with a very slender
721 configuration and the tendency to fail by elastic buckling. The Euler elastic critical
722 slenderness limit, as given in $\pi EI/(KL)^2$ is also highlighted in Figs. 24 and 25.

723 # 7. Conclusions

724 The local buckling induced fracture of concentrically loaded bracing members under
725 ELCF was investigated. A ductile fracture model was introduced into FE models with a
726 corresponding damage evolution rule to consider the nonlinear damage accumulation and the
727 load reversal effect during cyclic loading. The established FE models were validated against
728 the test results on CHS and SHS bracing members from three different test programmes.
729 ELCF fracture accompanied by large plastic deformation was assessed. The combined effects
730 of buckling and ductile fracture on the deformation capacity and the fracture life were
731 quantified in terms of the normalized cross-sectional slenderness and global slenderness,
732 using plastic-hinge based analytical models at different stages. The following conclusions can
733 be drawn from this study:

734 1. FE models were developed incorporating the modified Mohr-Coulomb (MMC)
735 fracture criterion and damage evolution rule at the material level, and these could
736 accurately predict the buckling induced fracture under ELCF for bracing members
737 with different cross-sections and manufacturing processes.
738 2. The geometric parameters, i.e. cross-sectional and global slenderness, had different
739 effects on the global and localized deformation capacity. Bracing members with

stocky cross-sections and high member slenderness tended to possess superior global deformation capacity to members composed of slender cross-sections.

3. The hot-rolled tubes exhibited obvious benefits in deformation capacity compared with their cold-formed counterparts after local buckling. A prediction model for the localized strain at the maximum compressive displacement before fracture, which offered satisfactory degree of accuracy, was proposed.
4. The brace ductility prior to fracture was quantified using a rotation index. A prediction model for the rotation capacity was proposed and could provide accurate predictions of the maximum global rotation values. This prediction model was applied to a structure-level study combined with a simplified analytical model of a one-story braced frame. Based on the parametric study, it is suggested to consider the coupling effects of local and global buckling when developing the cross-sectional slenderness limits for a bracing member designed for a specified deformation capacity.
5. Some bracing members with low global and sectional (less than λ_{hd}) slenderness values suffered from severe local buckling and could not meet the 0.04 rad story drift angle demand of the highly-ductile members in AISC 341-10.
6. Hot-rolled members under extreme seismic actions should satisfy the cross-sectional limit for highly-ductile members in the AISC seismic design provisions, in order to reap the benefits from the hot-rolling manufacturing process.

Acknowledgments

The authors are grateful for the support from the Chinese National Engineering Research Centre for Steel Construction (Hong Kong Branch) at The Hong Kong Polytechnic University. The first author would like to thank the financial support from JSPS KAKENHI

764 Grant Number 19F19360. Support from Dr. K.H. Nip for providing the essential
765 experimental data is also gratefully appreciated.
766

Abbreviations

CF:	cold-formed
CHS:	circular hollow section
CVGM:	cyclic void growth model
ECCS:	European Convention for Constructional Steelwork
ELCF:	extremely low cycle fatigue
EPFM:	elastic-plastic fracture mechanics
FE:	finite element
GTN:	Gurson-Tvergaard-Needleman
HF:	hot-finished
HR:	hot-rolled
HSFG:	high strength friction grip
LCF:	low cycle fatigue
LEFM:	linear-elastic fracture mechanics
MMC:	modified Mohr-Coulomb
RHS:	rectangular hollow section
SEM:	scanning electron microscope
SHS:	square hollow section
SWDM:	stress-weight damage model

References

[1] Tremblay R. Inelastic seismic response of steel bracing members. Journal of Constructional Steel Research 2002; 58(5-8):665-701.

[2] Fell BV. Large-scale testing and simulation of earthquake-induced ultra low cycle fatigue in bracing members subjected to cyclic inelastic buckling. Ph.D. thesis, University of California, Davis, 2008.

[3] Nip KH, Gardner L, Elghazouli AY. Cyclic testing and numerical modelling of carbon steel and stainless steel tubular bracing members. Engineering Structures 2010; 32(2):424-441.

[4] Nip KH, Gardner L, Elghazouli AY. Ultimate behaviour of steel braces under cyclic loading. Proceedings of the ICE - Structures and Buildings 2013; 166(5): 219-234.

[5] Sheehan T., Chan TM. Cyclic response of hollow and concrete-filled circular hollow section braces. Proceedings of the ICE – Structures and Buildings 2014; 167(3): 140-152.

[6] Elchalakani M, Zhao XL, Grzebieta R. Tests of cold-formed circular tubular braces under cyclic axial loading. ASCE Journal of Structural Engineering 2003; 129(4):507-514.

[7] Packer JA, Chiew SP, Tremblay R, Martinez-Saucedo G. Effect of material properties on hollow section performance. Proceedings of the ICE - Structures and Buildings 2010; 163(6):375-390.

[8] Uriz P. Towards earthquake resistant design of concentrically braced steel structures. Ph.D. Thesis, University of California, Berkeley, 2005.

[9] Nip KH. Cyclic behaviour of carbon steel and stainless steel tubular members. Ph.D. thesis. Imperial College London, UK, 2009.

[10] Coffin JL. A study of the effect of cyclic thermal stresses on a ductile metal. Am Soc Mech Eng 1954; 76:931-50.

[11] Manson SS. Behaviour of materials under conditions of thermal stress. NACA TN 2933; 1953.

[12] Wen HJ, Mahmoud H. A new approach to predict cyclic response and fracture of shear links and eccentrically braced frames. Frontiers in Built Environment 2018; (4): 11.

[13] Kanvinde, AM. Predicting Fracture in Civil Engineering Steel Structures: State of the Art. Journal of Structural Engineering 2016; 143: 03116001.

[14] Kanvinde AM, Deierlein GG. Cyclic void growth model to assess ductile fracture initiation in structural steels due to ultra low cycle fatigue. Journal of engineering mechanics 2007; 133(6): 701-712.

[15] Bai YL. Fracture of 1045 steel under complex loading history. AIP Conf. Proc. Vol. 1383, 58-746: 2011.

[16] Algarni M, Choi Y, Bai YL. A unified material model for multiaxial ductile fracture and extremely low cycle fatigue of Inconel 718. International Journal of Fatigue 2017; 96: 162-177.

[17] Pack K, Marcadet S. Numerical failure analysis of three-point bending on martensitic hat assembly using advanced plasticity and fracture models for complex loading. International Journal of Solids and Structures 2016; 85:144-159.

[18] Wen HJ, Mahmoud H. New model for ductile fracture of metal alloys. II: Reverse loading. Journal of Engineering Mechanics 2015; 142(2): 04015089.

[19] McClintock FA. A criterion for ductile fracture by the growth of holes. Journal of applied mechanics 1968; 35: 363-371.

[20] Rice JR, Tracey DM. On the ductile enlargement of voids in triaxial stress fields. Journal of the Mechanics and Physics of Solids 1969; 17: 201-217.

[21] Gurson AL. Continuum theory of ductile rupture by void nucleation and growth: Part I - Yield criteria and flow rules for porous ductile media. Journal of engineering materials and technology 1977; 99: 2-15.

[22] Needleman A, Tvergaard VF. An analysis of ductile rupture in notched bars. Journal of the Mechanics and Physics of Solids 1984; 32: 461-490.

[23] Tresca H. Comptes Rendus Acad Sci 1864; 59: 754.

[24] Bai YL, Wierzbicki T. A new model of metal plasticity and fracture with pressure and Lode dependence. International journal of plasticity 2008; 24(6): 1071-1096.

[25] Bai YL, Wierzbicki T. Application of extended Mohr–Coulomb criterion to ductile fracture. International Journal of Fracture 2010; 161(1): 1-20.

[26] Johnson GR, Cook WH. Fracture characteristics of three metals subjected to various strains, strain rates, temperatures and pressures. Engineering fracture mechanics 1985; 21(1): 31-48.

[27] Bao YB, Wierzbicki T. On fracture locus in the equivalent strain and stress triaxiality space. International Journal of Mechanical Sciences 2004; 46(1): 81-98.

[28] Xue L, Wierzbicki T. Ductile fracture initiation and propagation modeling using damage plasticity theory. Engineering Fracture Mechanics 2008; 75(11): 3276-3293.

852 [29] Barsoum I, Jonas F. Rupture mechanisms in combined tension and shear -Experiments.
853 International Journal of Solids and Structures 2007; 44(6): 1768-1786.
854 [30] Kiran R, Khandelwal K. A triaxiality and Lode parameter dependent ductile fracture
855 criterion. Engineering Fracture Mechanics 2014; 128: 121-138.
856 [31] Barsoum I, Faleskog J. Rupture mechanisms in combined tension and shear—
857 Micromechanics. International Journal of Solids and Structures 2007; 44(17): 5481-
858 5498.
859 [32] Barsoum I, Faleskog J. Micromechanical analysis on the influence of the Lode
860 parameter on void growth and coalescence. International Journal of Solids and
861 Structures 2011; 48(6): 925-938.
862 [33] Danas K, Castañeda P. Influence of the Lode parameter and the stress triaxiality on the
863 failure of elasto-plastic porous materials. International Journal of Solids and Structures
864 2012; 49: 1325-1342.
865 [34] Brünig M, Gerke S, Hagenbrock V. Micro-mechanical studies on the effect of the stress
866 triaxiality and the Lode parameter on ductile damage. International Journal of Plasticity
867 2013; 50: 49-65.
868 [35] Smith, CMA. Stress-Weighted Damage Model for Ductile Fracture Initiation in
869 Structural Steel under Cyclic Loading and Generalized Stress States. Ph.D. thesis,
870 Stanford University, 2013.
871 [36] AISC 341. Seismic provisions for structural steel buildings. AISC-341, Chicago, 2010.
872 [37] Tateishi, K, Hanji T, Minami K. A prediction model for extremely low cycle fatigue
873 strength of structural steel. International Journal of fatigue 2007; 29(5): 887-896.
874 [38] Kuroda M. Extremely low cycle fatigue life prediction based on a new cumulative
875 fatigue damage model. International Journal of Fatigue 2002; 24(6): 699-703.
876 [39] Xue L. A unified expression for low cycle fatigue and extremely low cycle fatigue and
877 its implication for monotonic loading. International Journal of Fatigue 2008; 30(10-11):
878 1691-1698.
879 [40] Wen HJ, Mahmoud H. New model for ductile fracture of metal alloys. I: Monotonic
880 loading. Journal of Engineering Mechanics 2015; 142(2): 04015088.
881 [41] Hosford W. A generalized isotropic yield criterion. J Appl Mech 1972; 39:607.
882 [42] Hollomon JH. Tensile Deformation. Transactions of the Metallurgical Society of AIME
883 1945; 162:268-290.
884 [43] Swift HW. Plastic instability under plane stress. Journal of the Mechanics and Physics
885 of Solids 1952; 1(1): 1-18.

886 [44] Bao YB, Wierzbicki T. On the cut-off value of negative triaxiality for fracture.
887 Engineering fracture mechanics 2005; 72(7): 1049-1069.
888 [45] ASTM. Standard Specification for Pipe, Steel, Black and Hot-dipped, Zinc-coated,
889 Welded and Seamless. ASTM A53/A53M-12, West Conshohocken, ASTM
890 international; 2012.
891 [46] ECCS. Recommended testing procedure for assessing the behaviour of structural steel
892 elements under cyclic loads. European Convention for Constructional Steelwork 1986,
893 Brussels, Belgium.
894 [47] ABAQUS 6.14 [Computer software]. Dassault Systems, Waltham, MA, USA; 2014.
895 [48] Hibbitt HD, Karlsson BI, Sorensen P. ABAQUS documentation collection. Ver. 6.14,
896 USA; 2014.
897 [49] Lemaitre J, Chaboche JL, Mechanics of Solid Materials, Cambridge University Press,
898 1990.
899 [50] Xu F, Chen J, Chan TM. Mechanical behaviour of concrete-filled CHS connections
900 subjected to in-plane bending. Engineering Structures 2017; 148: 101-112.
901 [51] Xu F, Chen J, Chan TM. Numerical analysis and punching shear fracture based design
902 of longitudinal plate to concrete-filled CHS connections. Construction and Building
903 Materials 2017; 156: 91-106.
904 [52] Xu F, Chen J, Jin WL. Punching shear failure of concrete-filled steel tubular CHS
905 connection. Journal of Constructional Steel Research 2016; 124: 113-121.
906 [53] Xu, F., Chen, J., Shu, K. and Su, M.N. Cyclic behaviour of double-tube buckling-
907 restrained braces for boiler steel plant structures. Journal of Constructional Steel
908 Research 2018, 150: 556-569.
909 [54] Wierzbicki T, Bao YB, Lee YW, Bai YL. Calibration and evaluation of seven fracture
910 models. International Journal of Mechanical Sciences 2005; 47(4): 719-743.
911 [55] Bai YL, and Atkins T. Tension and shear cracking during indentation of ductile
912 materials by opposed wedges. Engineering Fracture Mechanics 2012; 96: 49-60.
913 [56] Teng X. Numerical prediction of slant fracture with continuum damage mechanics.
914 Engineering Fracture Mechanics 2008; 75(8): 2020-2041.
915 [57] Nip KH, Gardner L, Davies CM, Elghazouli AY. Extremely low cycle fatigue tests on
916 structural carbon steel and stainless steel. Journal of Constructional Steel Research
917 2010; 66(1): 96-110.

[58] Takeuchi T, Matsui R. Cumulative cyclic deformation capacity of circular tubular braces under local buckling. ASCE Journal of Structural Engineering 2011; 137(11):1311-1318.

[59] Timoshenko SP, James MG. Theory of elastic stability. 2nd Edition, McGraw Hill, 1961.

[60] Sheehan T. Cyclic behaviour of hollow and concrete-filled circular hollow section braces. PhD thesis, University of Warwick, 2013.

[61] Tremblay R, Archambault MH, Filiatrault A. Seismic response of concentrically braced steel frames made with rectangular hollow bracing members. Journal of Structural Engineering 2003; 129(12): 1626-1636.

[62] AISC 341. Seismic provisions for structural steel buildings. AISC-341, Chicago, 2016.

List of Figure Captions

Fig. 1 Types of coordinate system in the space of principal stresses [24]

Fig. 2 Test specimens and loading protocols

Fig. 3 Comparison of hysteresis curves for CHS brace tests [5] (FEA refers to Finite Element Analysis)

Fig. 4 Comparison of hysteresis curves for SHS brace tests [3] (a~c: HR; e~g: CF)

Fig. 5 Comparison of failure mode of CHS brace specimen HF-H-1500 [5]

Fig. 6 Different failure modes of SHS brace specimens [3]

Fig. 7 FE model of a quarter of specimen

Fig. 8 Effect of element types of C3D8R and S4R on the hysteretic response and fracture

Fig. 9 Initiation and propagation of cyclic fracture cracks

Fig. 10 Mesh sensitivity study (CF-H-1500)

Fig. 11 Typical uniaxial stress-strain curve with progressive damage degradation [48] (Note: D refers to D_{post})

Fig. 12 Effect of damage accumulative parameter on hysteretic response and fracture (CF-H-1500)

Fig. 13 Relationship between fracture index and (a) stress triaxiality; (b) normalized Lode

Fig. 14 Flow chart for the USDFLD of the fracture model

Fig. 15 Analytical model at onset of local buckling

Fig. 16 Analytical model at maximum deformation before fracture

Fig. 17 Global angle parameter, θ_1

Fig. 18 Plastic hinge length, L_{H_G}

Fig. 19 Local angle parameter, θ_2

Fig. 20 Plastic hinge length, L_{H_L}

Fig. 21 Comparison of maximum compressive strain prior to fracture between calculation and FEA results

Fig. 22 Schematic illustration of simplified approach to evaluate the story drift angle in a one-story Chevron braced frame and plastic hinge model for brace (CHS)

Fig. 23 Global angle parameter, θ_3 at maximum compressive displacement prior to fracture

Fig. 24 Maximum allowable ductility level for brace facture

Fig. 25 Section and members limits for CHS brace based on story drift angle

List of Table Captions

Table 1. Summary of nominal dimensions and measured material properties of brace specimens

Table 2. Comparison between test and FE results

Table 3. Parameters of plastic model used in FE models

Table 4. Parameters of fracture criterion and damage evolution rule used in FE models

Table 5. Simulation matrix in parametric studies

Table 6. Parameters of proposed models

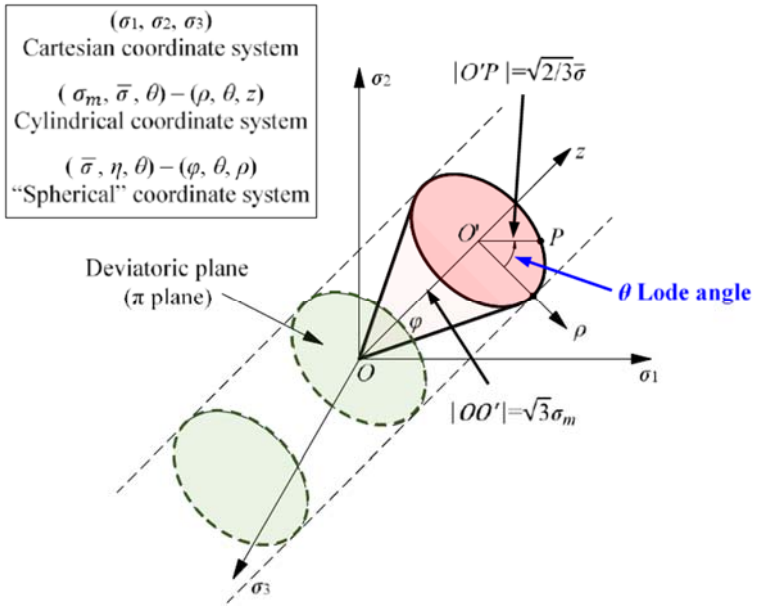


Fig. 1 Types of coordinate system in the space of principal stresses [24]

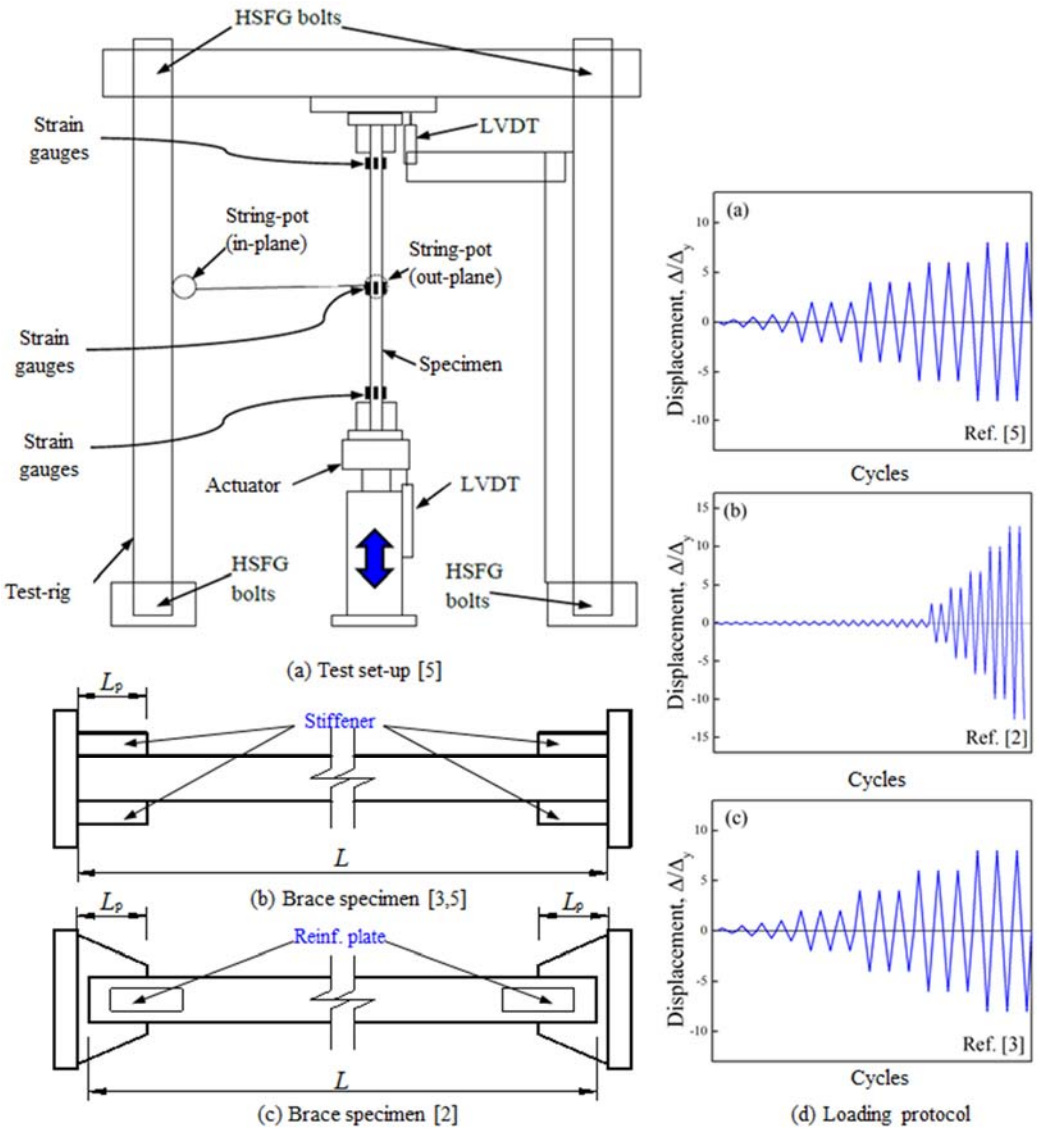
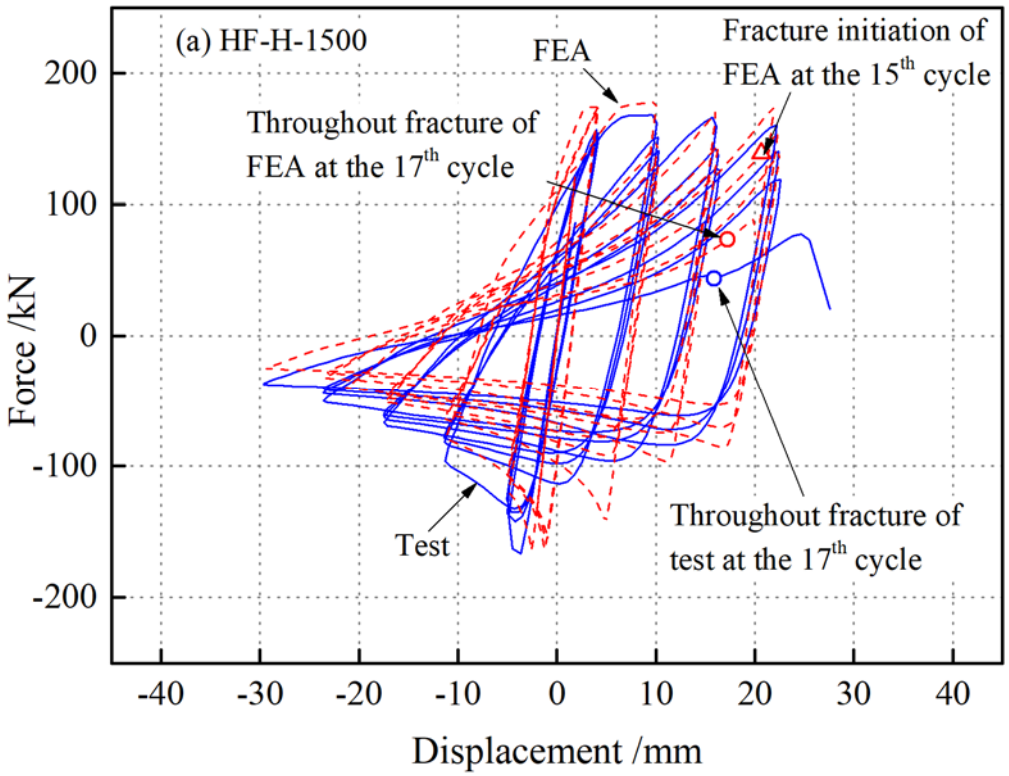
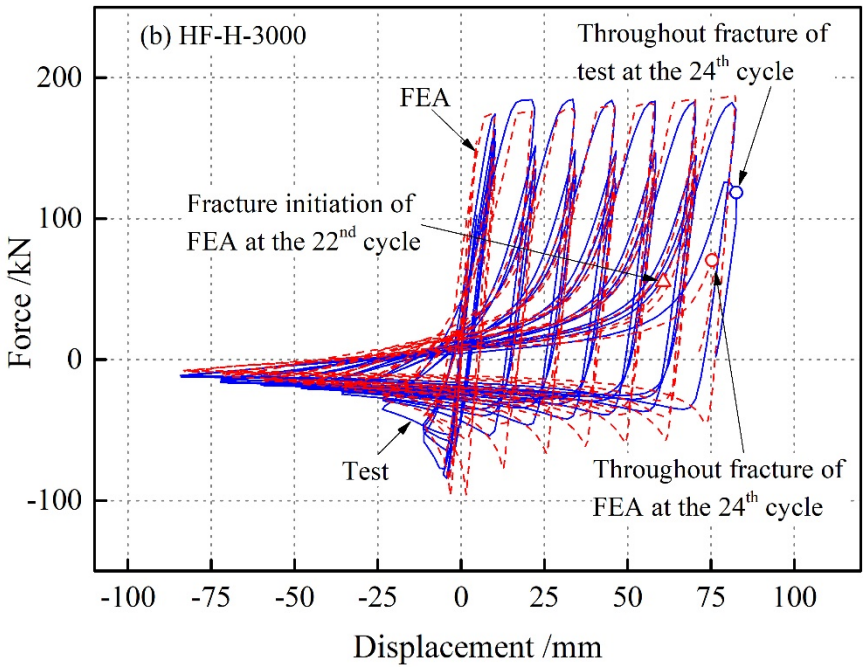


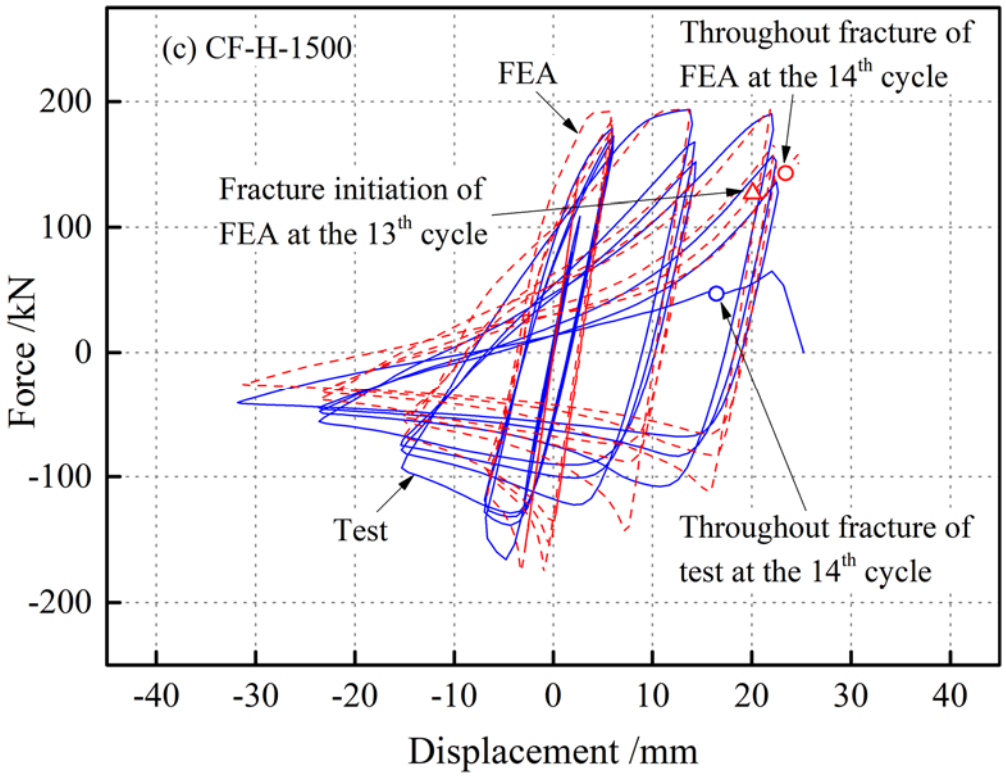
Fig. 2 Test specimens and loading protocols



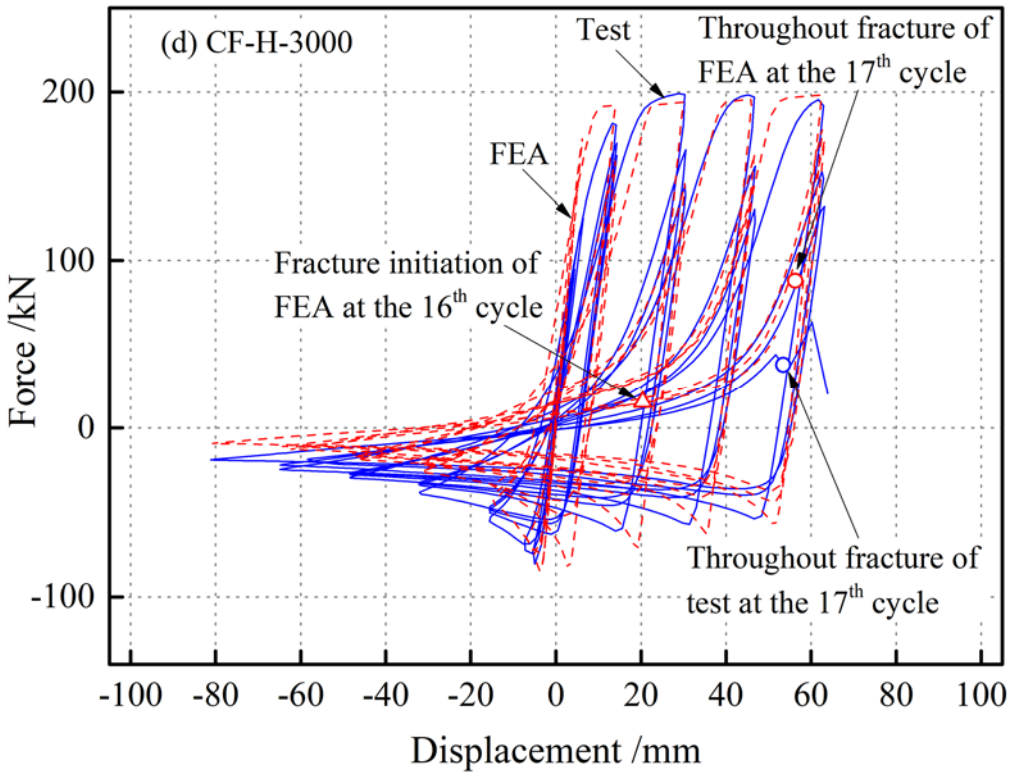
(a) HF-H-1500 (Hot-finished)



(b) HF-H-3000 (Hot-finished)

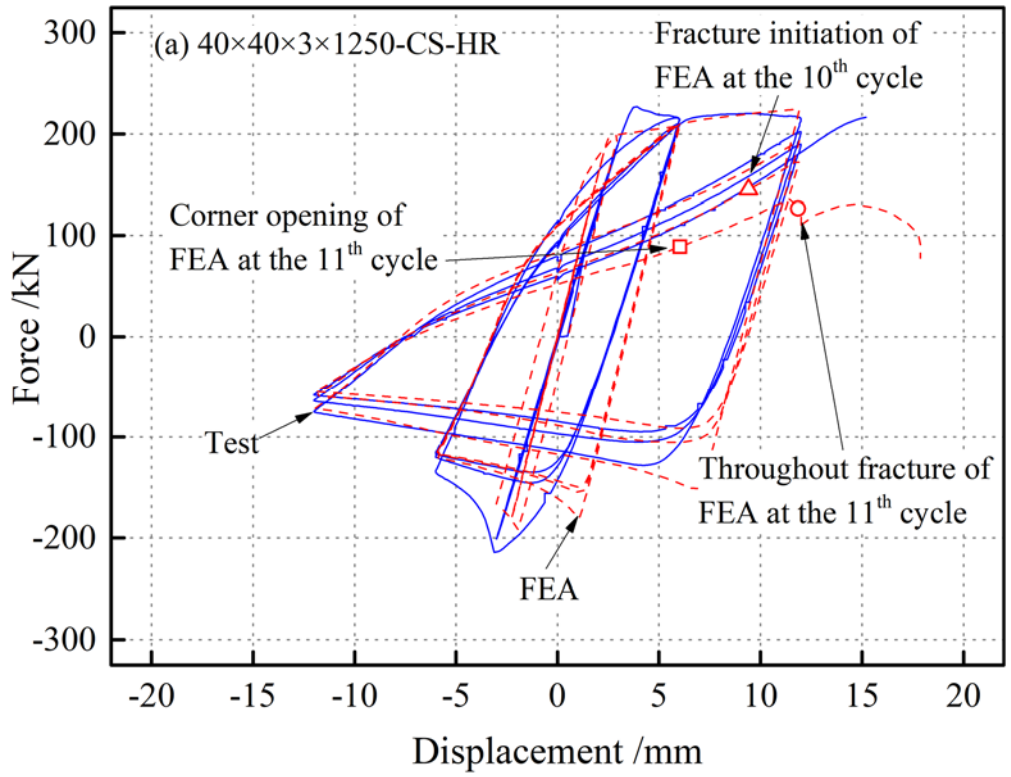


(c) CF-H-1500 (Cold-formed)

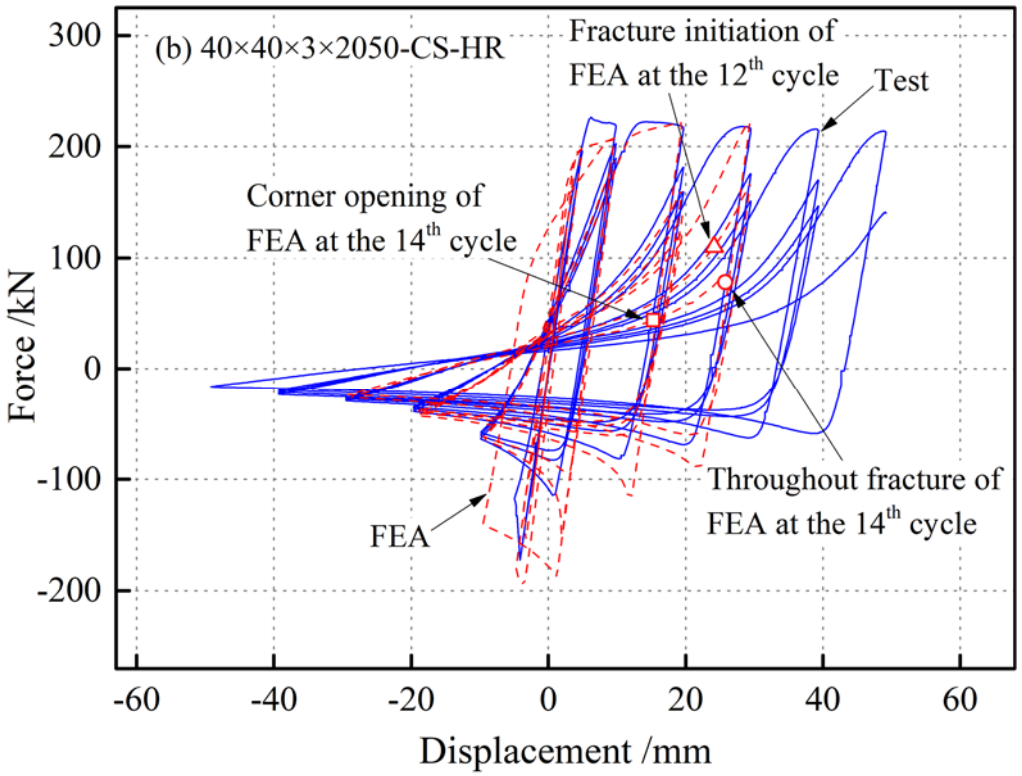


(d) CF-H-3000 (Cold-formed)

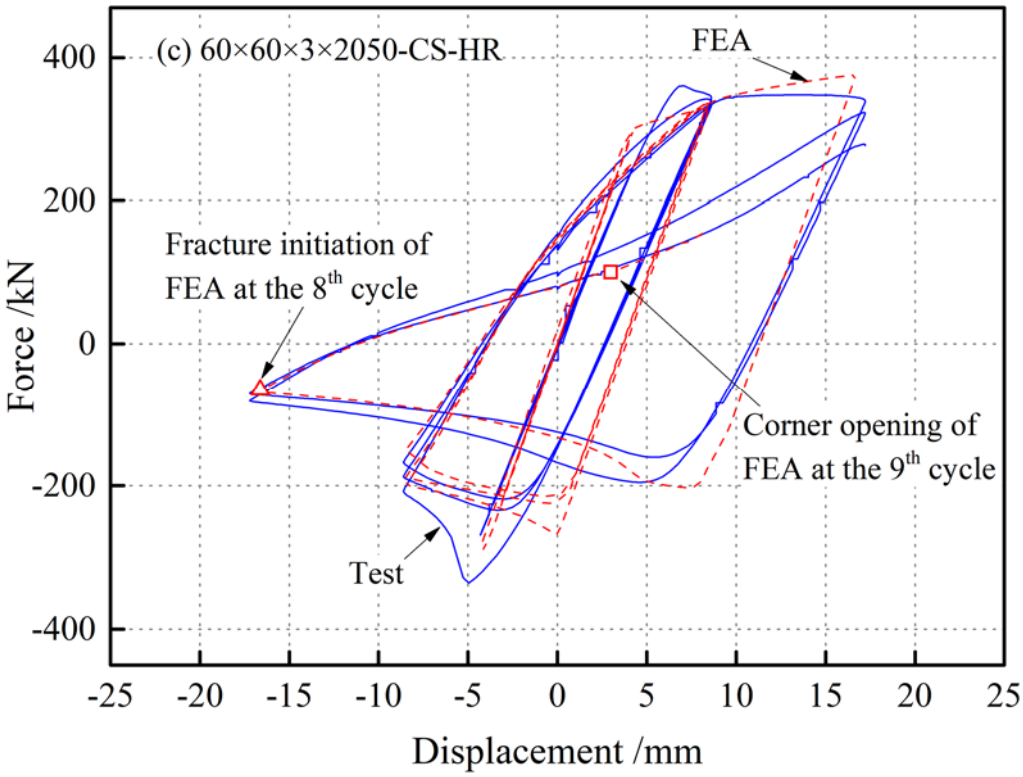
Fig. 3 Comparison of hysteresis curves for CHS brace tests [5] (FEA refers to Finite Element Analysis)



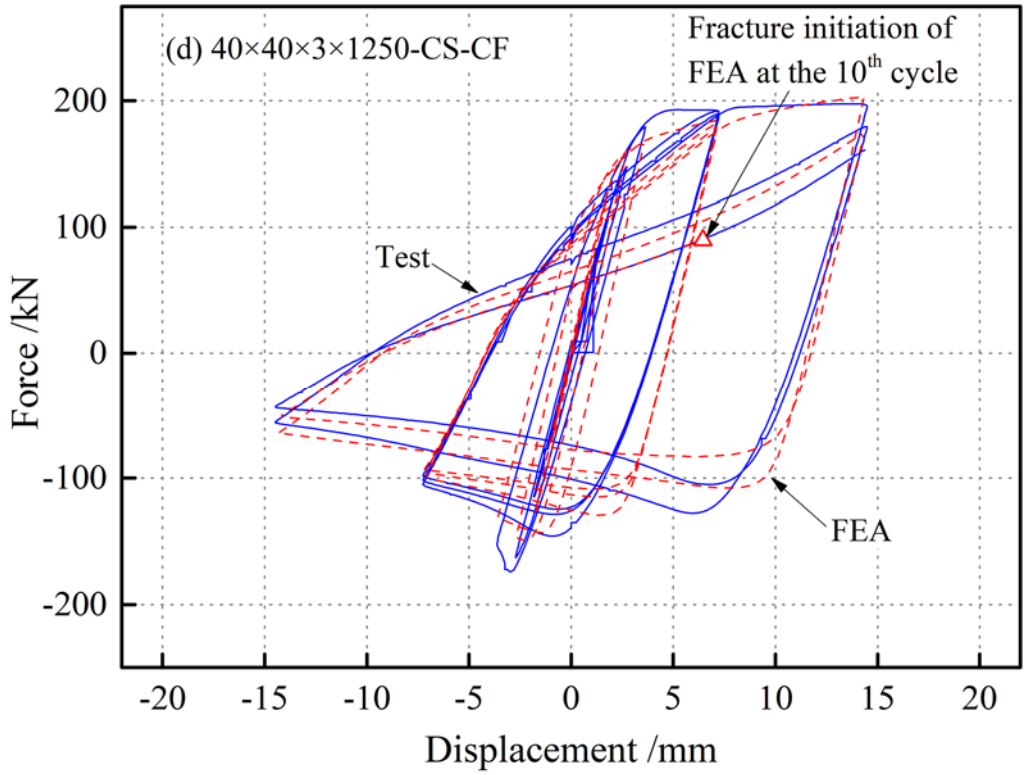
(a) 40×40×3×1250-CS-HR (Hot-rolled)



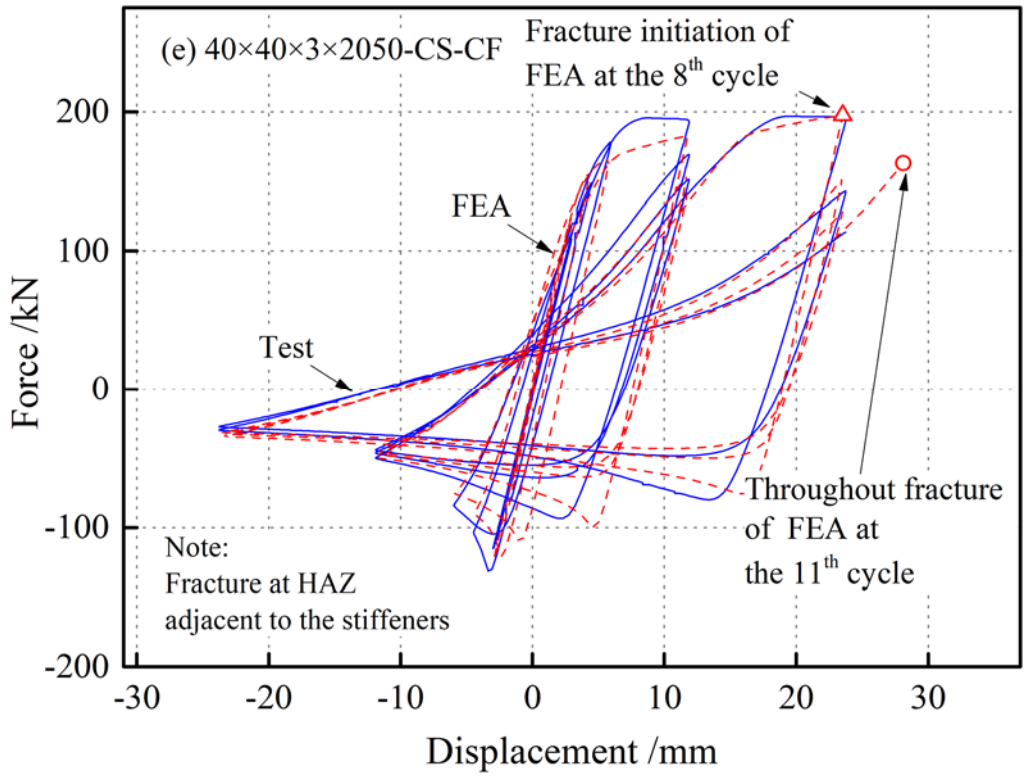
(b) 40×40×3×2050-CS-HR (Hot-rolled)



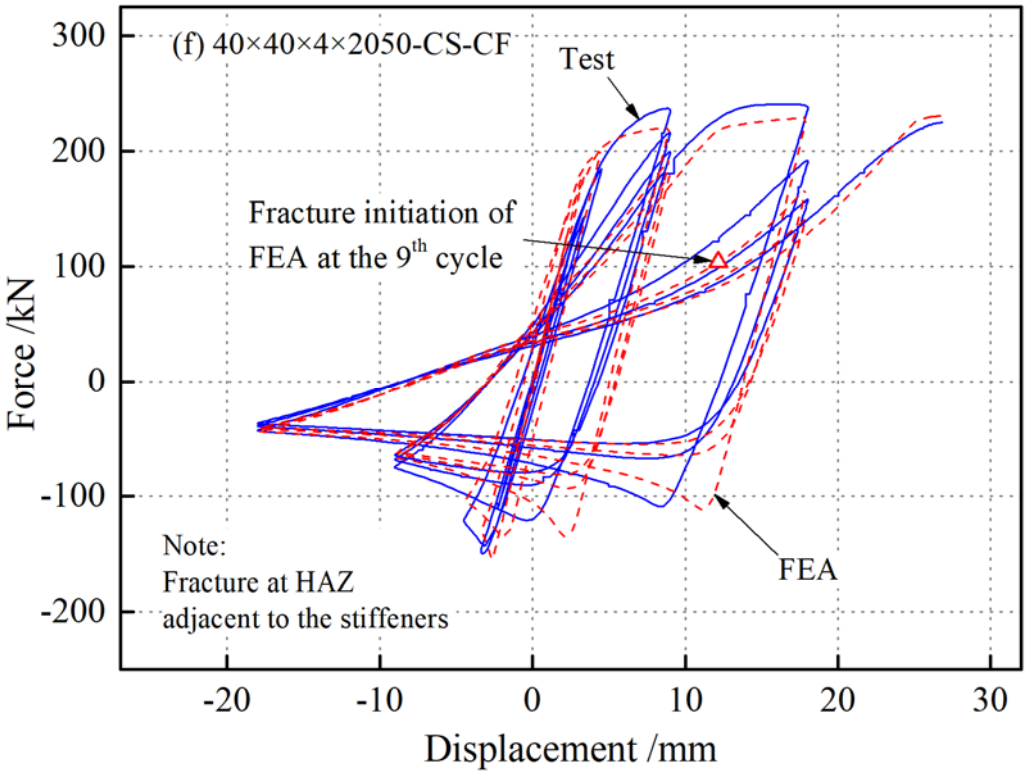
(c) 60×60×3×2050 -CS-HR (Hot-rolled)



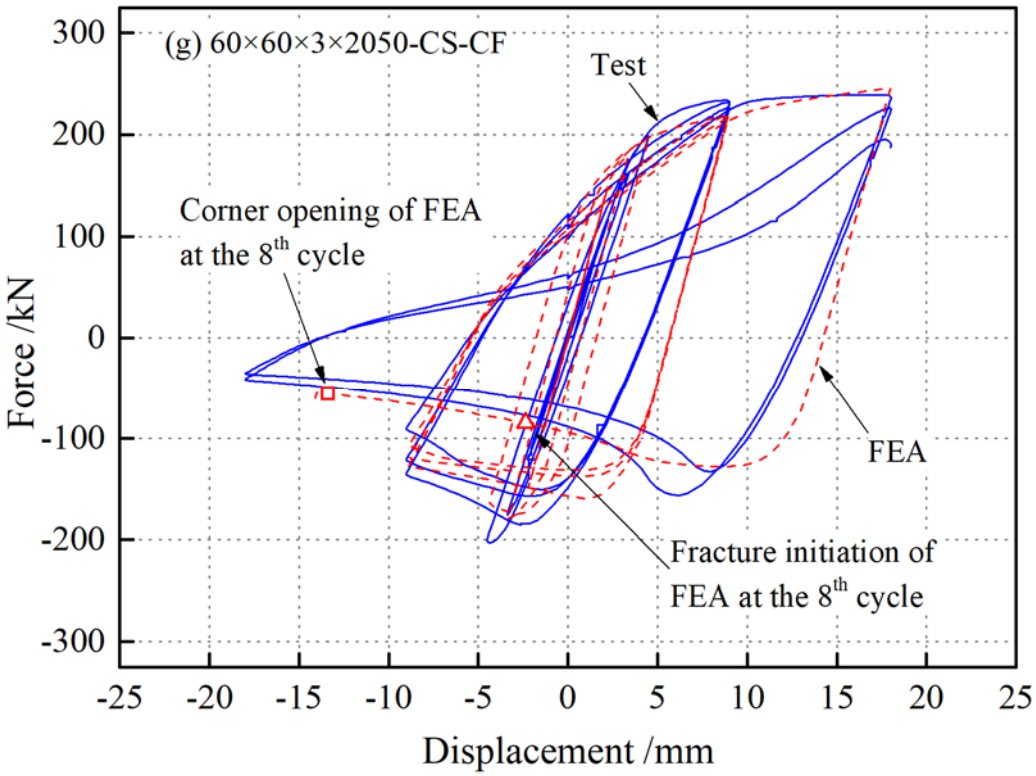
(d) 40×40×3×1250-CS-CF (Cold-formed)



(e) 40×40×3×2050-CS-CF (Cold-formed)

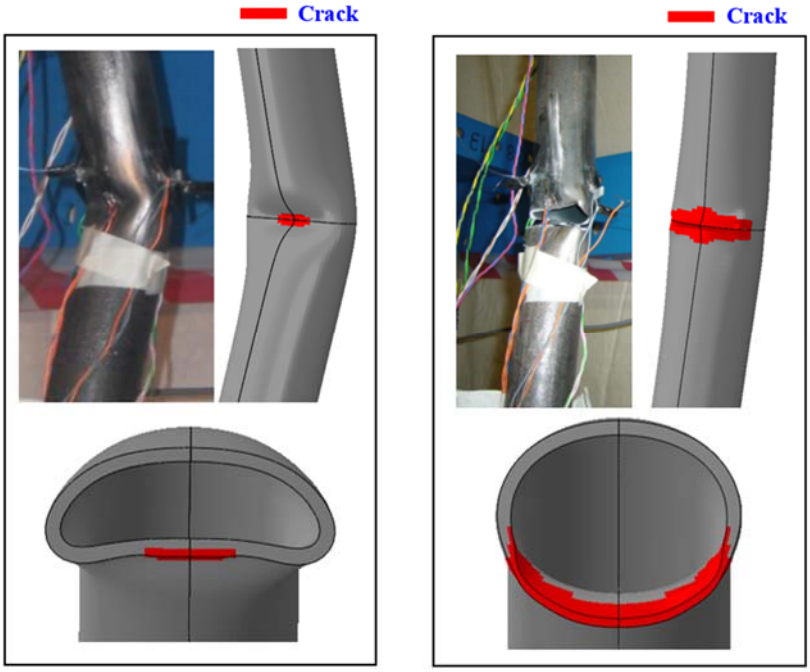


(f) 40×40×4×2050-CS-CF (Cold-formed)



(g) 60×60×3×2050-CS-CF (Cold-formed)

Fig. 4 Comparison of hysteresis curves for SHS brace tests [3] (a~c: HR; d~g: CF)



a) Fracture initiation b) Throughout fracture

Fig. 5 Comparison of failure mode of CHS brace specimen HF-H-1500 [5]

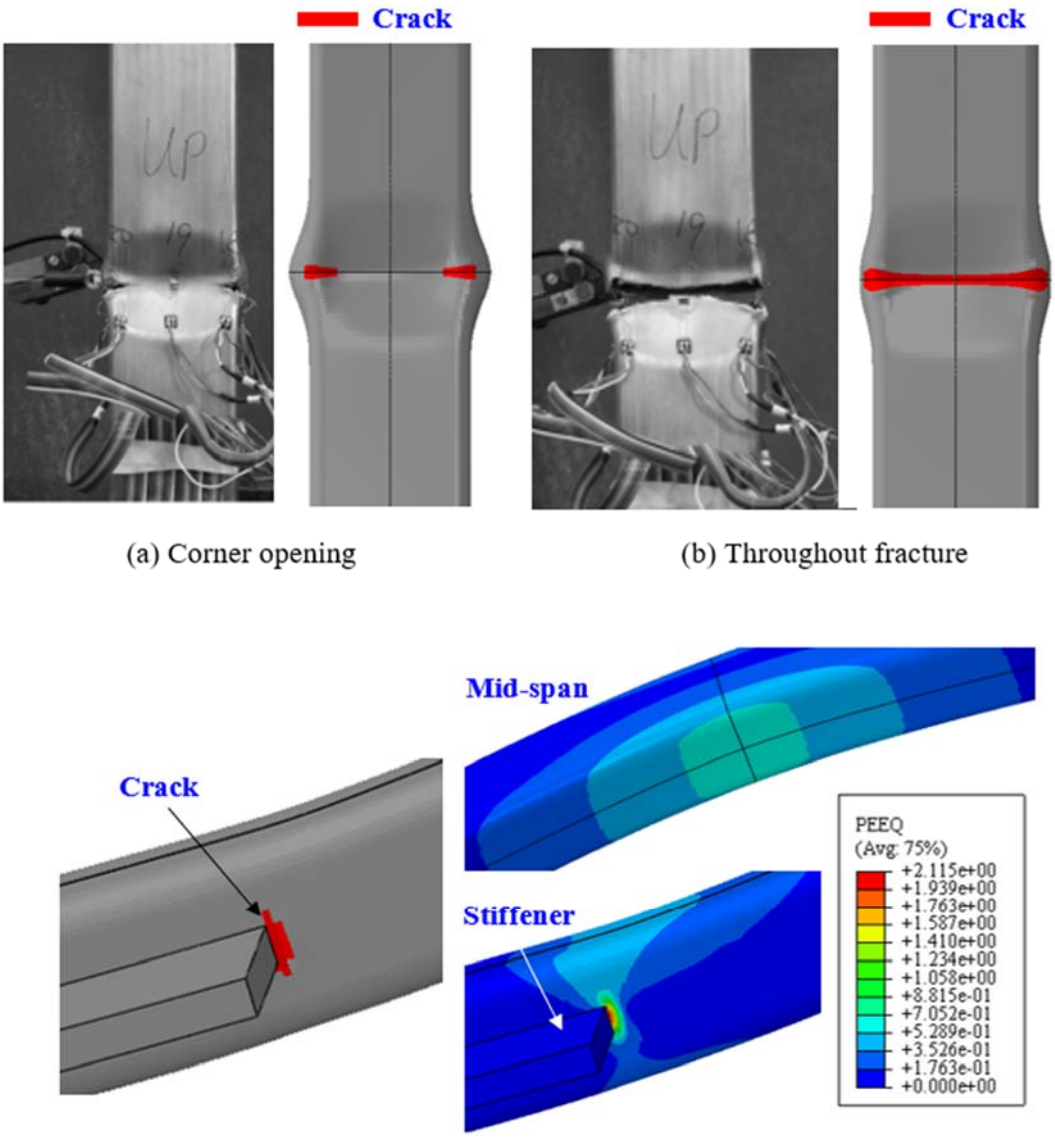


Fig. 6 Different failure modes of SHS brace specimens [3]
(a and b: Typical failure mode for fracture at mid-length - 60×60×3×2050-CS-HR;
c: typical failure mode for fracture around the stiffeners - 40×40×4×2050-CS-CF)

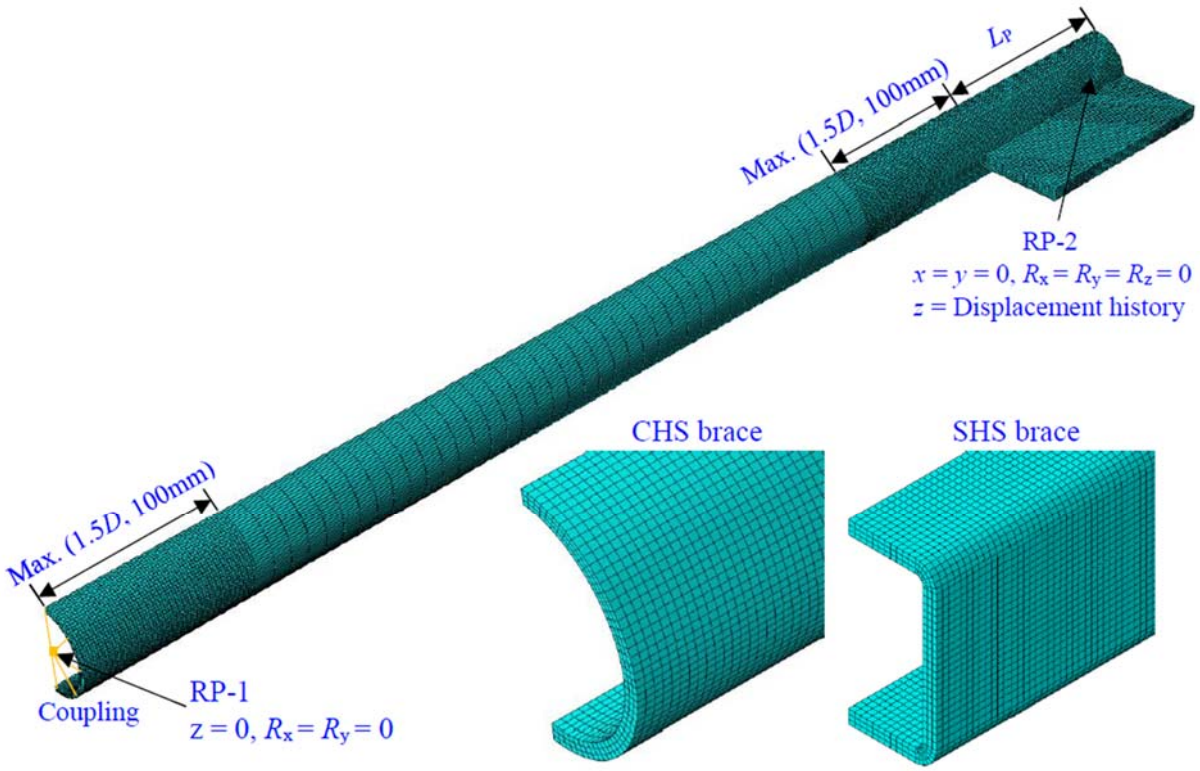
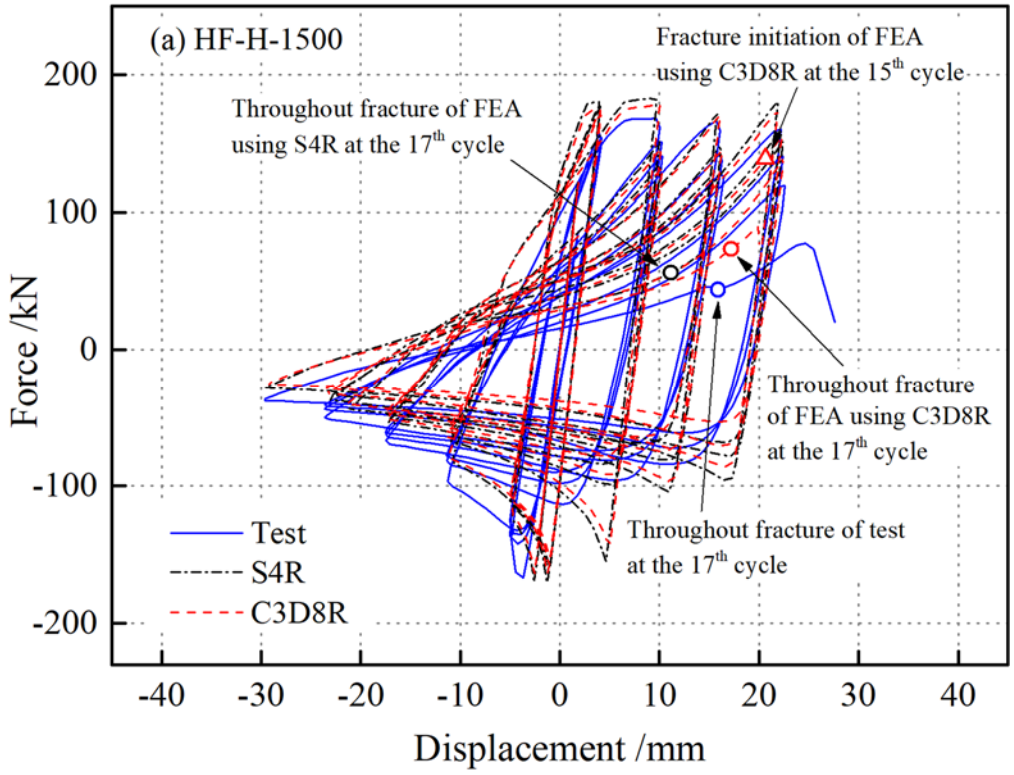
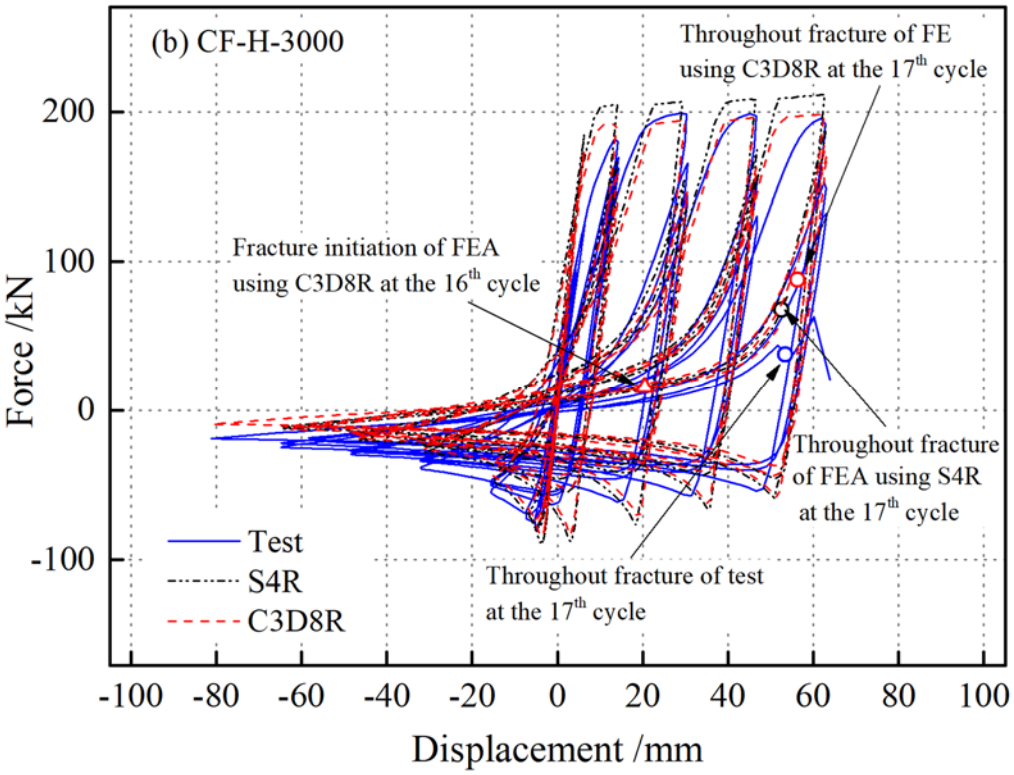


Fig. 7 FE model of a quarter of specimen



(a) HF-H-1500



(b) CF-H-3000

Fig. 8 Effect of element types of C3D8R and S4R on the hysteretic response and fracture

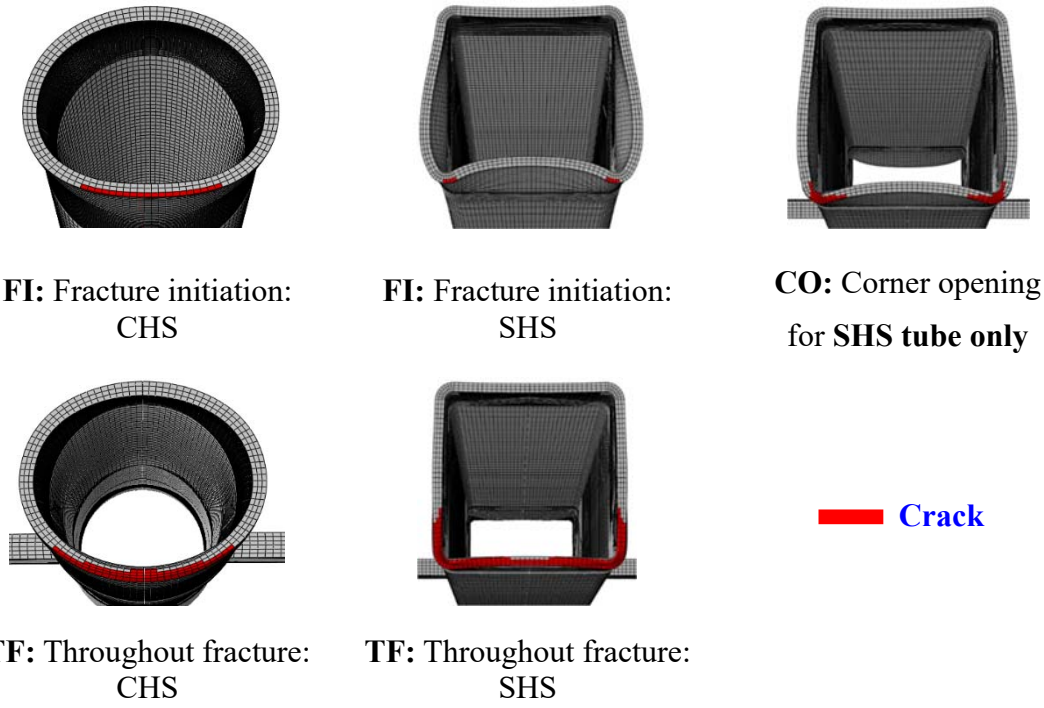


Fig. 9 Initiation and propagation of cyclic fracture cracks

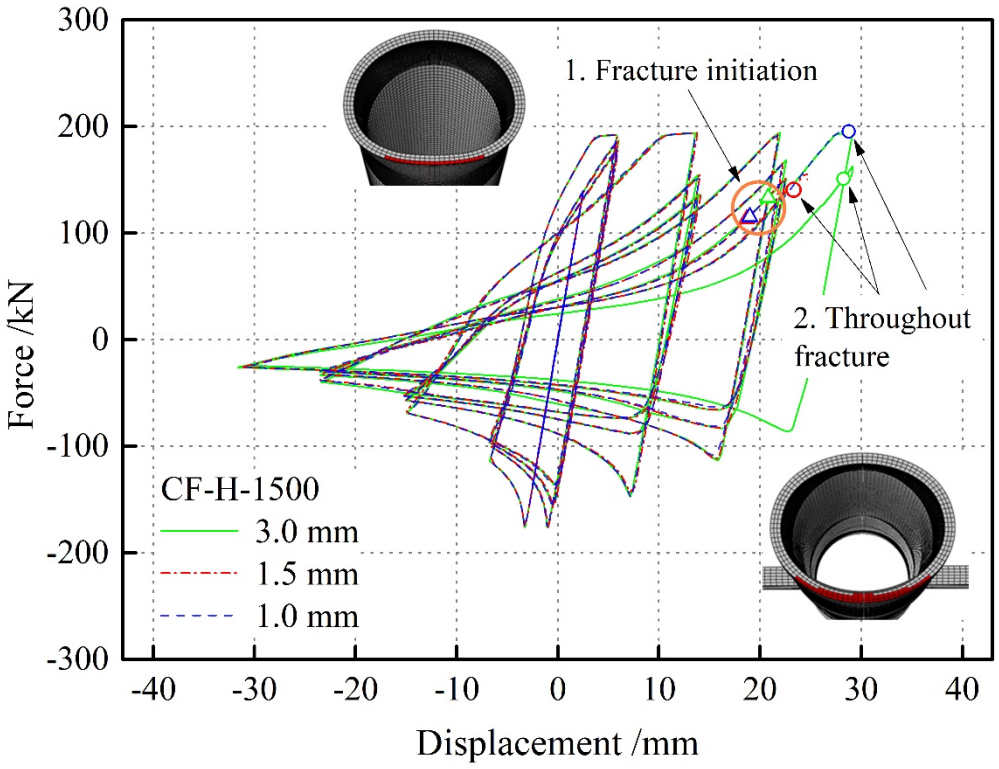


Fig. 10 Mesh sensitivity study (CF-H-1500)

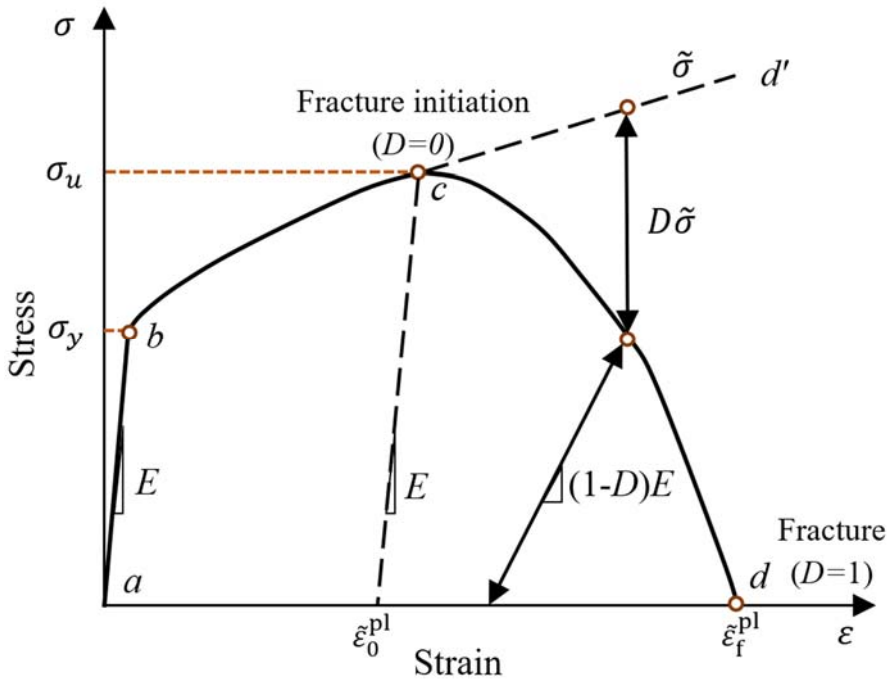


Fig. 11 Typical uniaxial stress-strain curve with progressive damage degradation [48] (Note: D refers to D_{post})

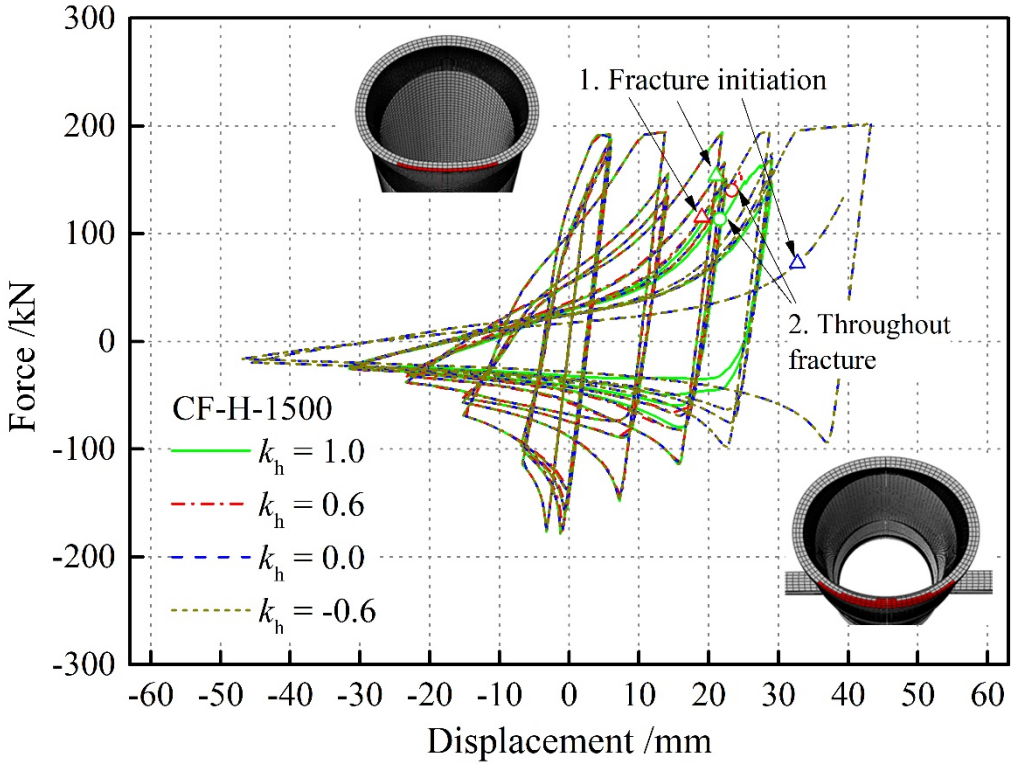
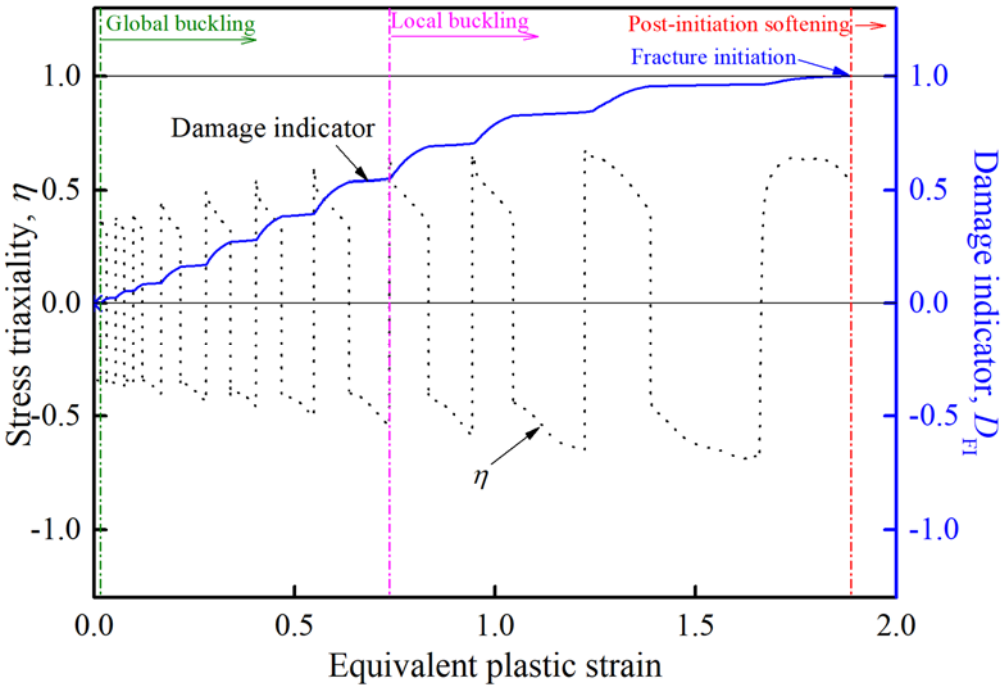
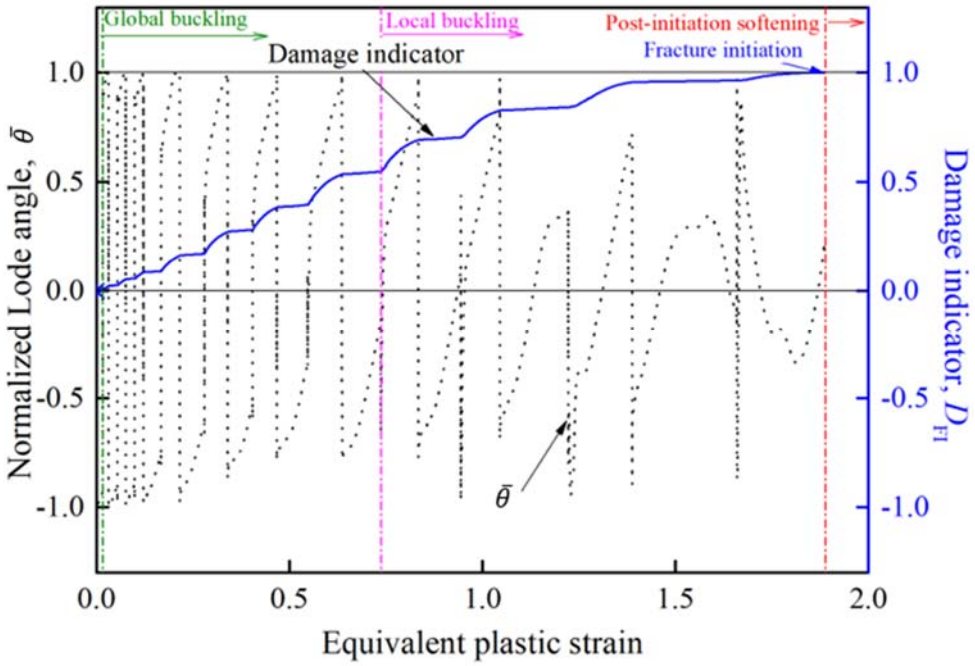


Fig. 12 Effect of damage accumulative parameter on hysteretic response and fracture (CF-H-1500)



a) Stress triaxiality



(b) Normalized Lode angle

Fig. 13 Relationship between fracture index and (a) stress triaxiality; (b) normalized Lode angle (HF-H-1500)

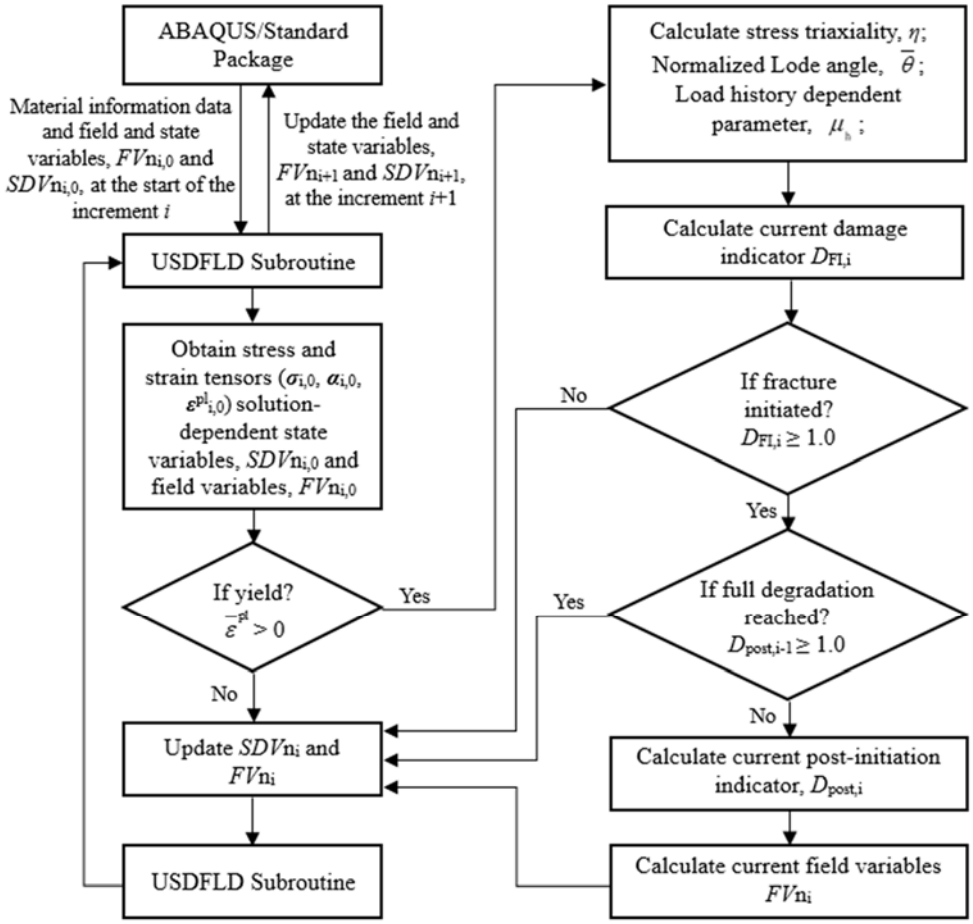
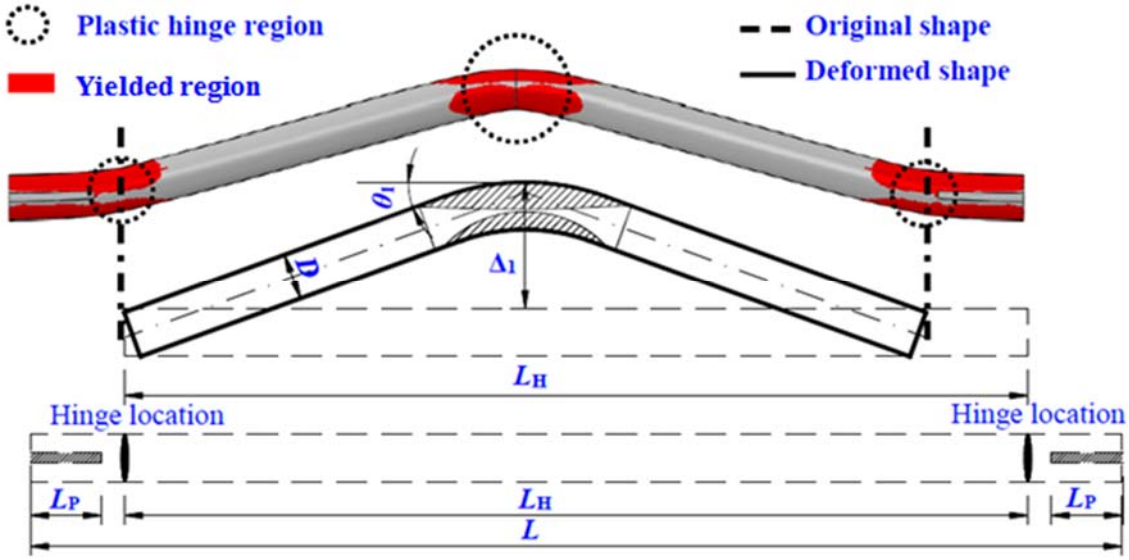
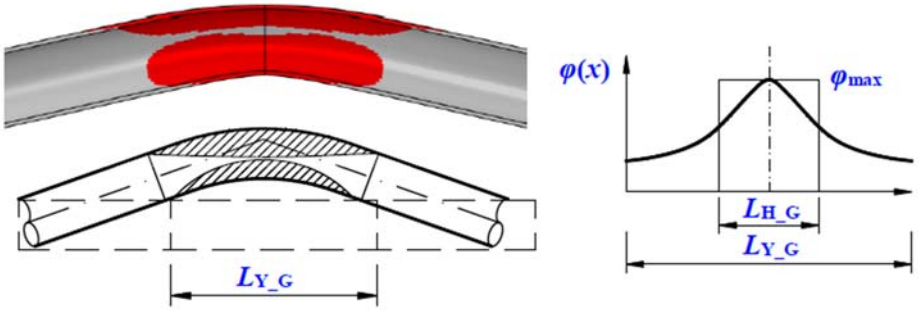


Fig. 14 Flow chart for the USDFLD of the fracture model

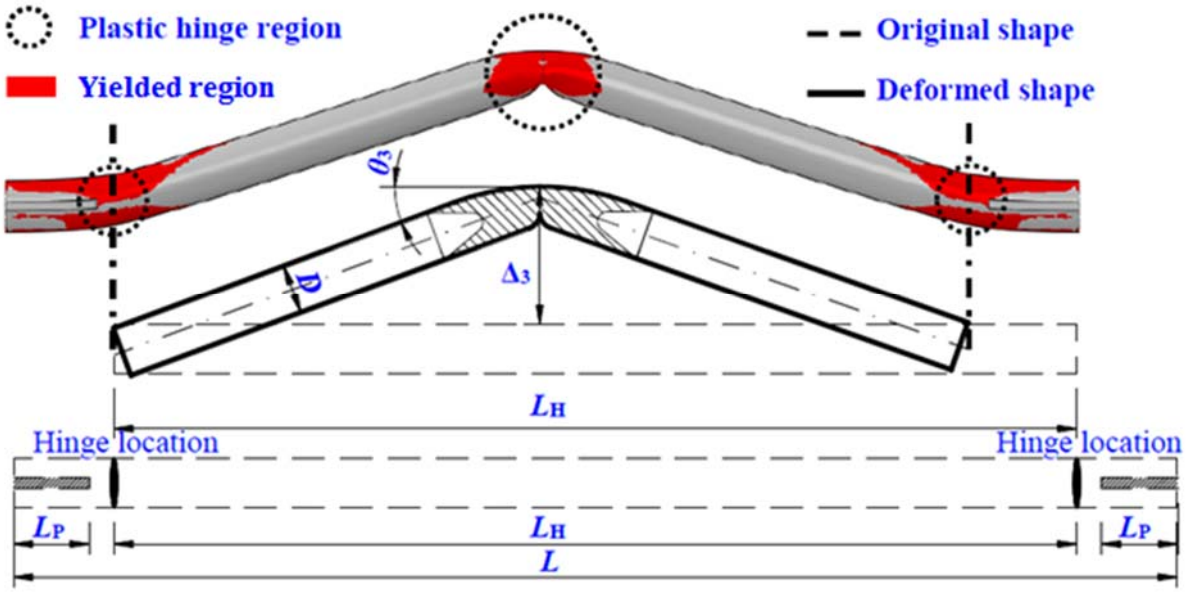


(a) Overall view

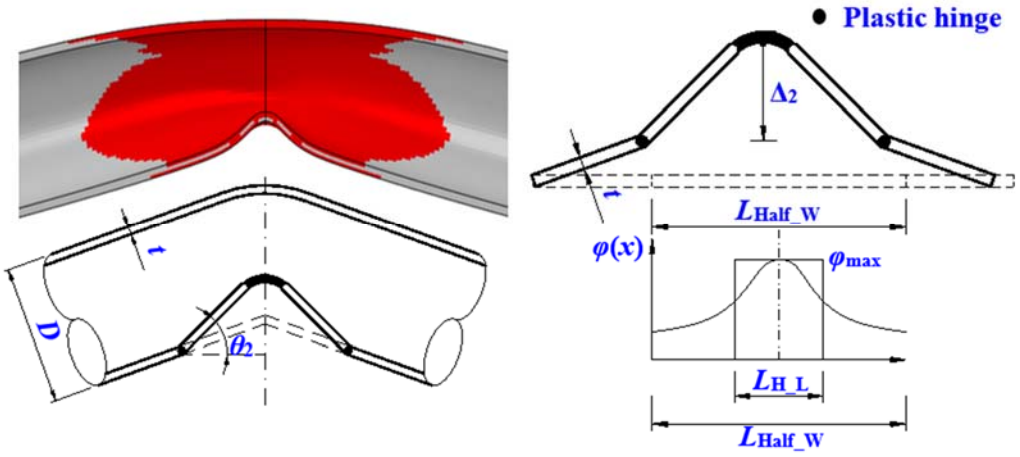


(b) Local view

Fig. 15 Analytical model at onset of local buckling

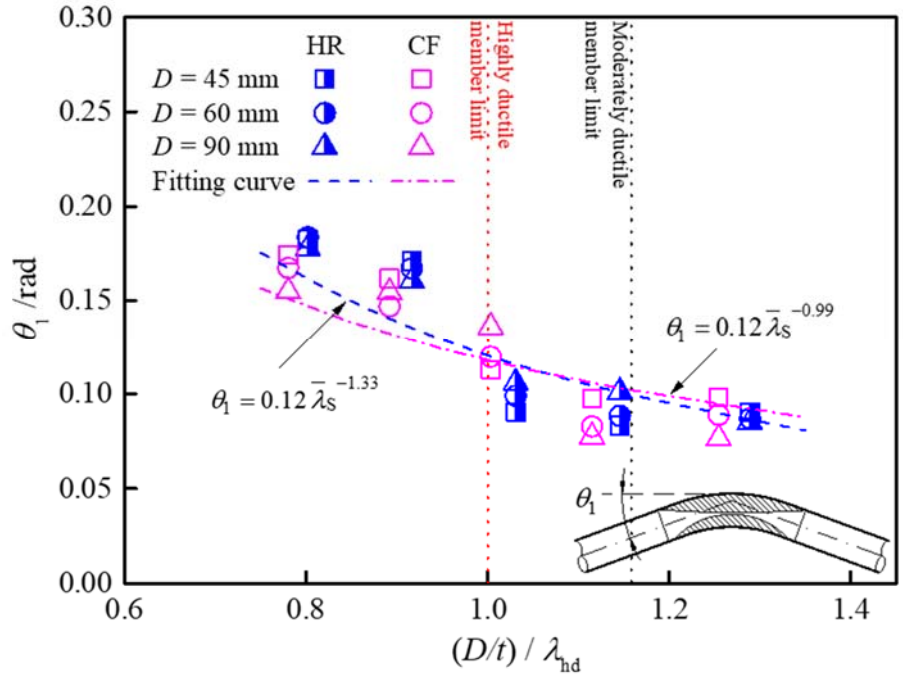


(a) Overall view

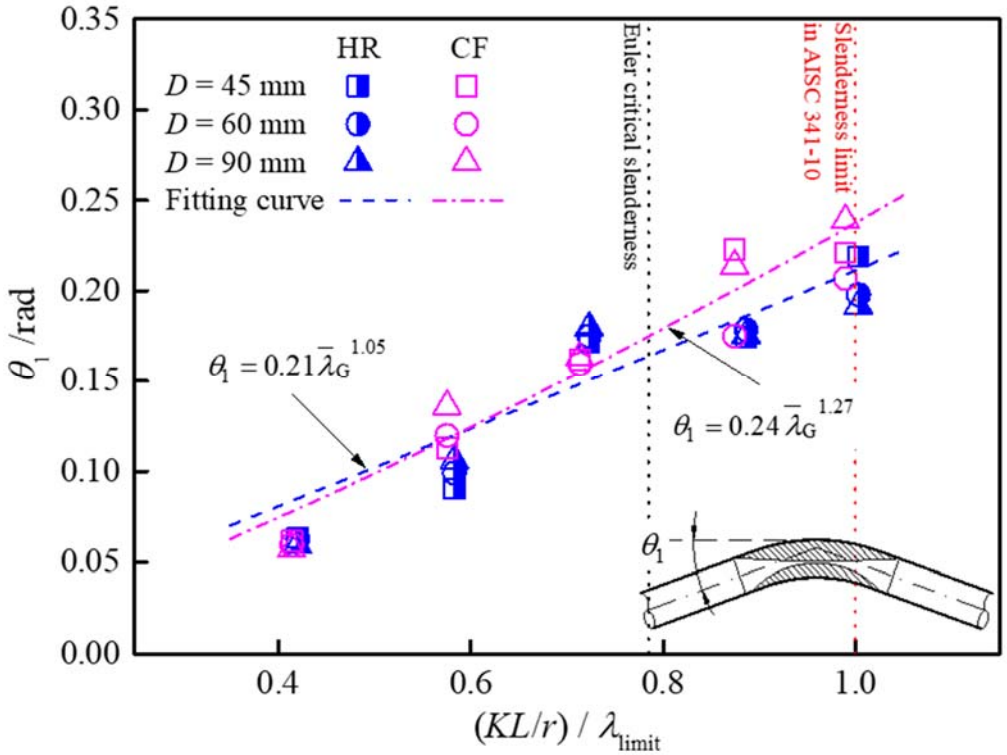


(b) Local view

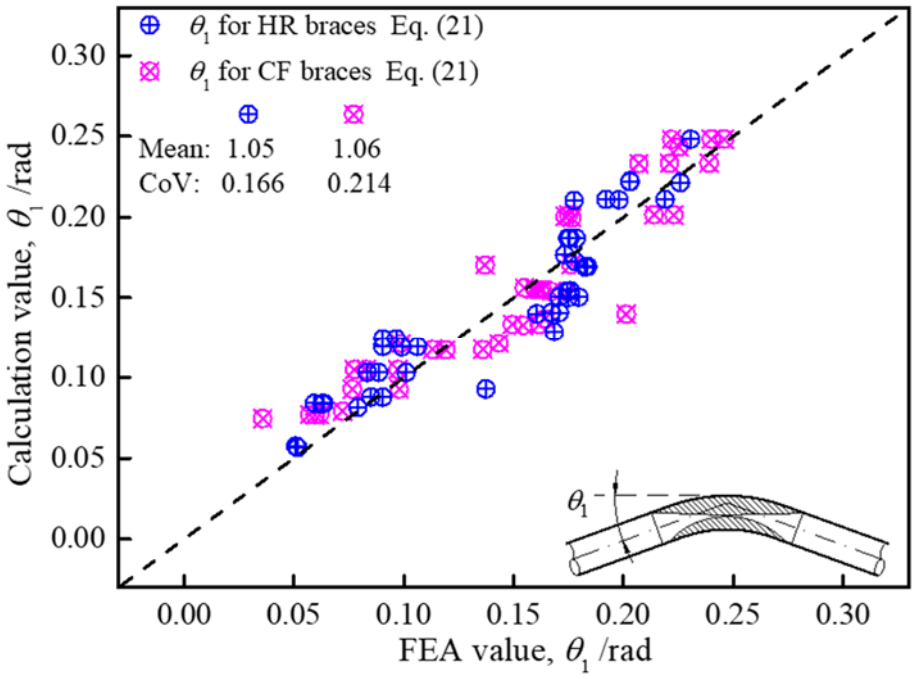
Fig. 16 Analytical model at maximum deformation before fracture



(a) $KL/r = 50$, $\bar{\lambda}_S = \dfrac{D/t}{\lambda_{hd}}$

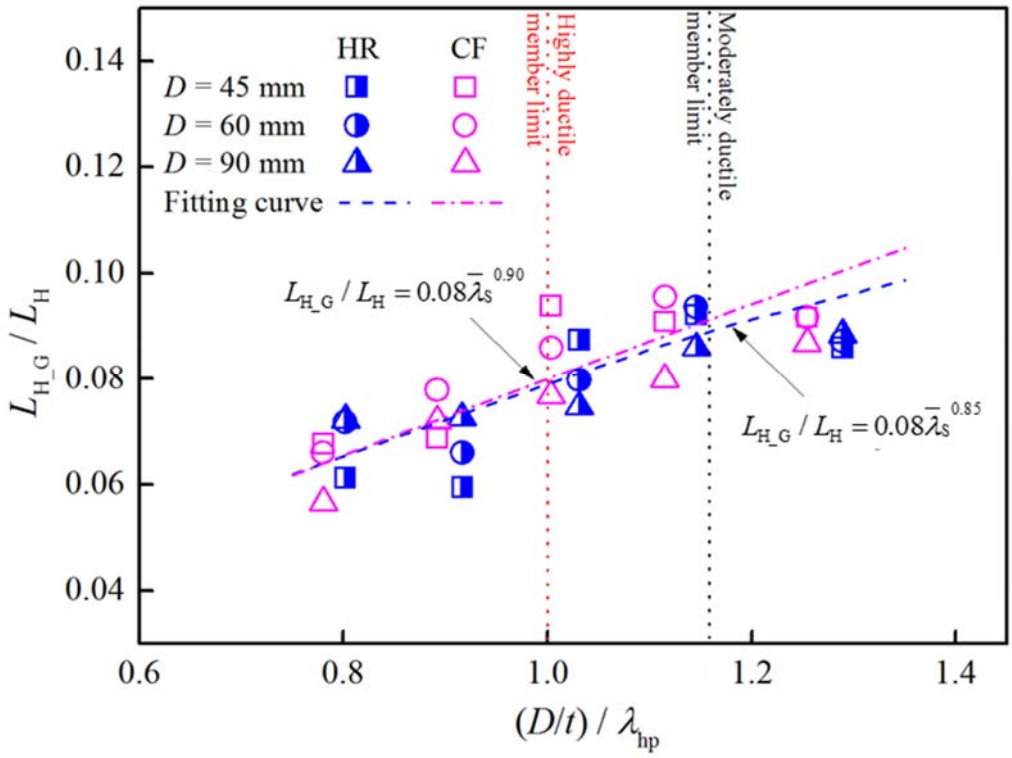


(b) $D/t = 18$, $\bar{\lambda}_G = \dfrac{KL/r}{\lambda_{limit}}$

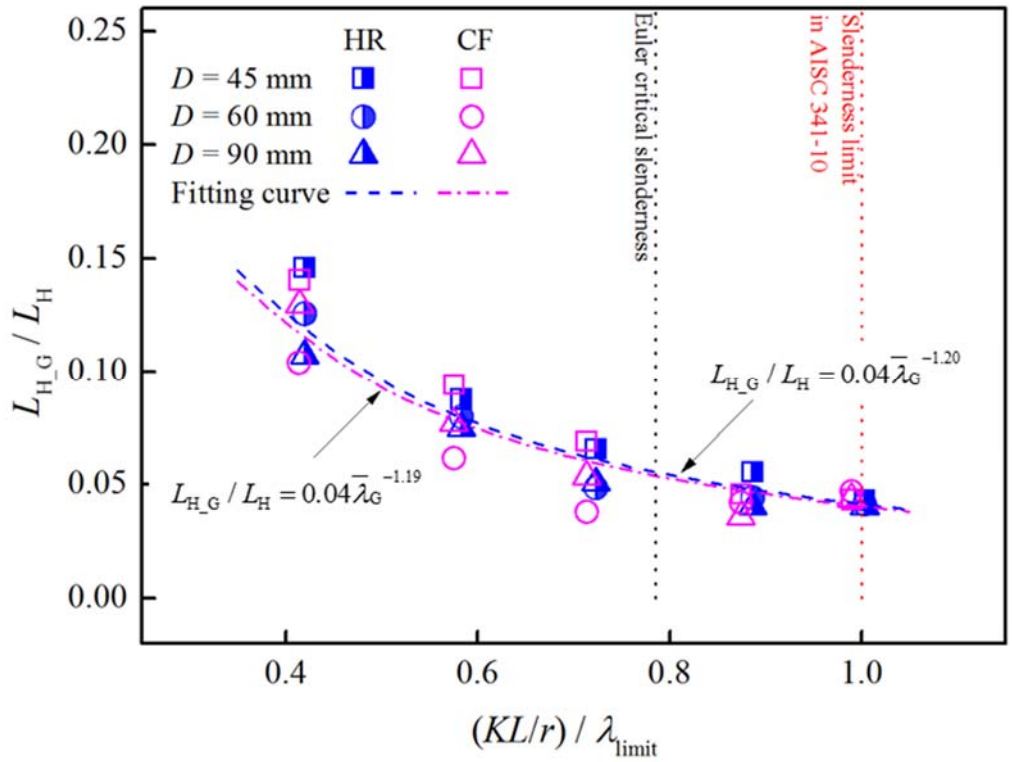


(c) Comparison between calculation and FEA results

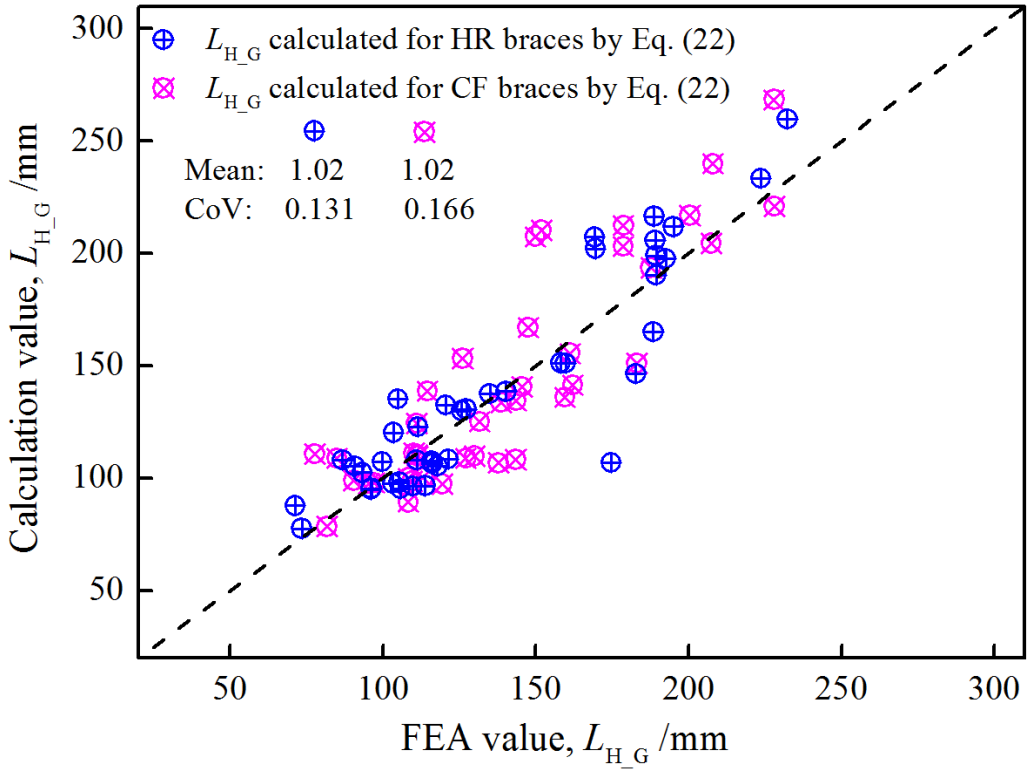
Fig. 17 Global angle parameter, θ_1



(a) $KL/r = 50$, $\bar{\lambda}_S = \dfrac{D/t}{\lambda_{hd}}$

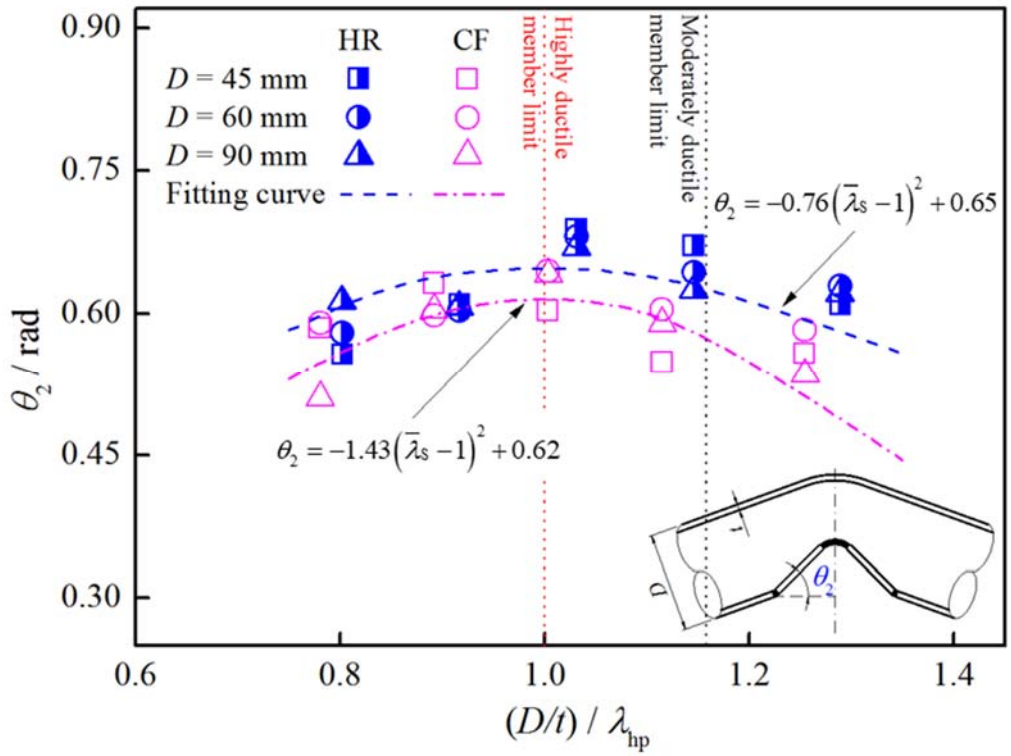


(b) $D/t = 18$, $\bar{\lambda}_G = \dfrac{KL/r}{\lambda_{limit}}$

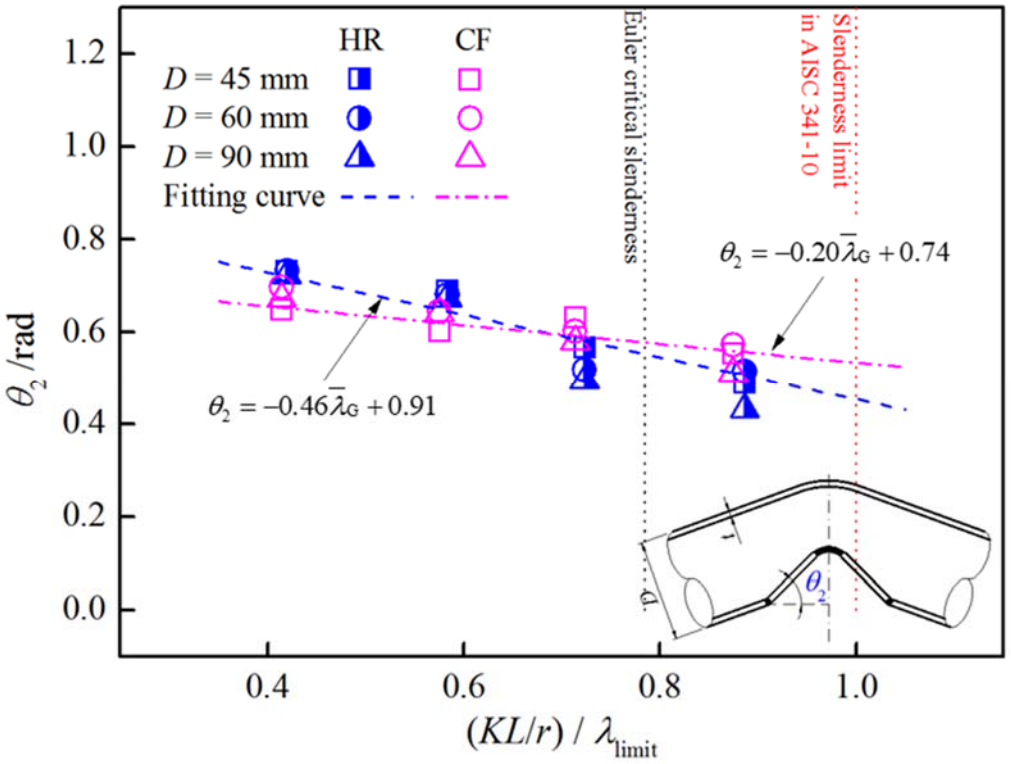


(c) Comparison between calculation and FEA results

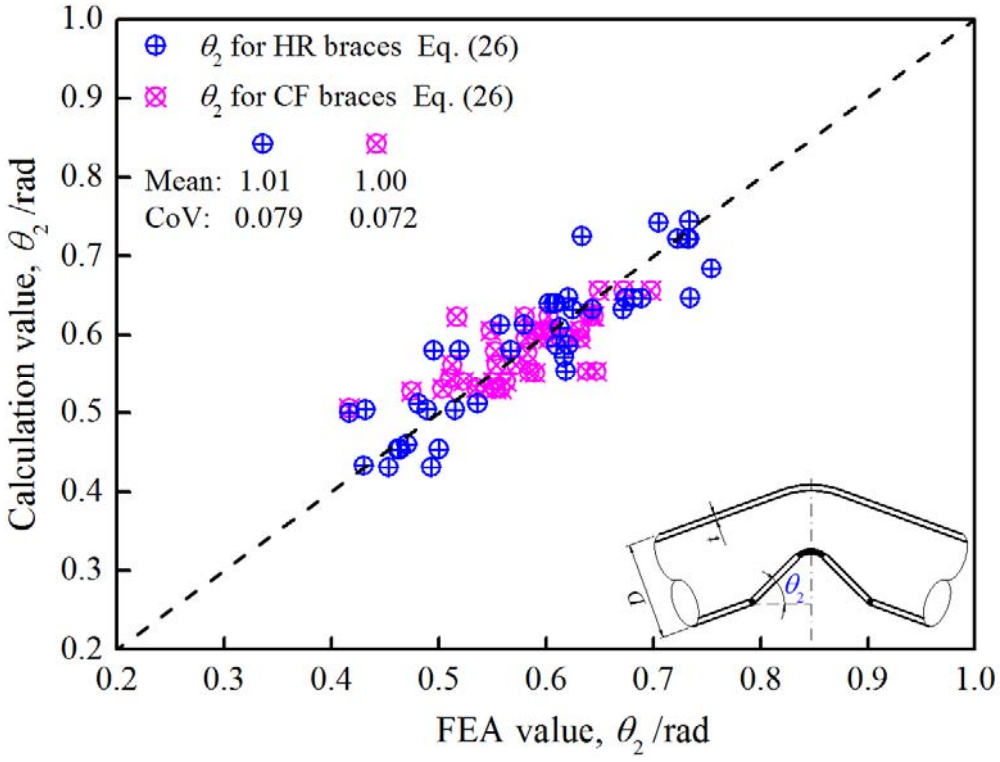
Fig. 18 Plastic hinge length, L_{H_G}



(a) $KL/r = 50$, $\bar{\lambda}_S = \dfrac{D/t}{\lambda_{hd}}$



(b) $D/t = 18$, $\bar{\lambda}_G = \dfrac{KL/r}{\lambda_{limit}}$



(c) Comparison between calculation and FEA results

Fig. 19 Local angle parameter, θ_2

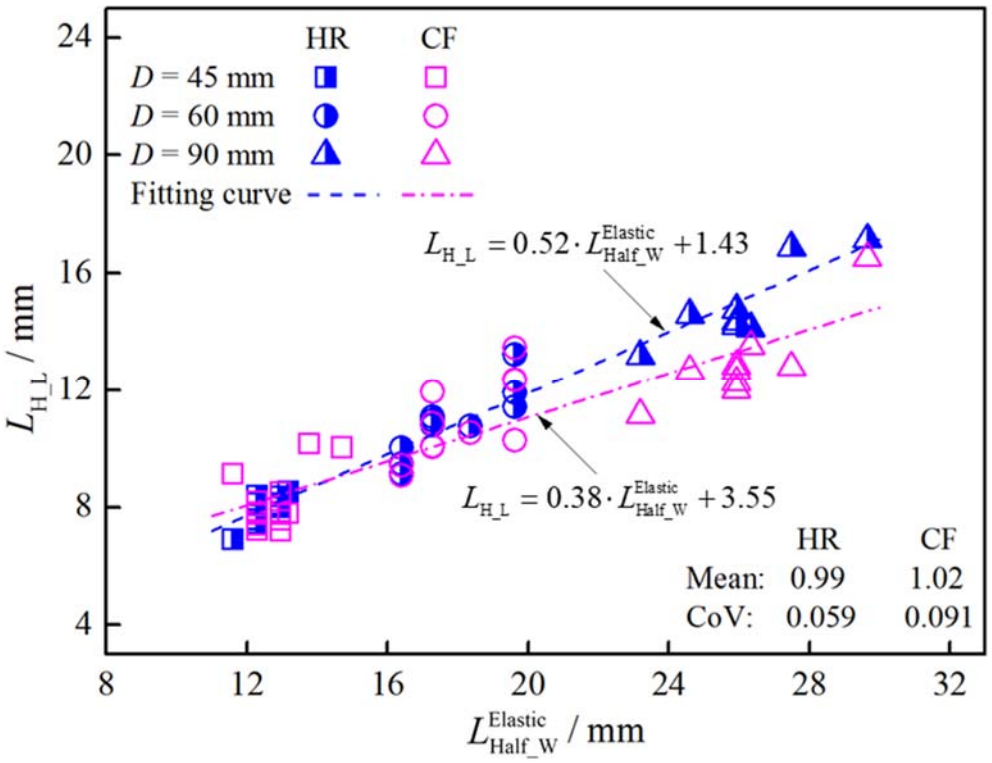


Fig. 20 Plastic hinge length, L_{H_L}

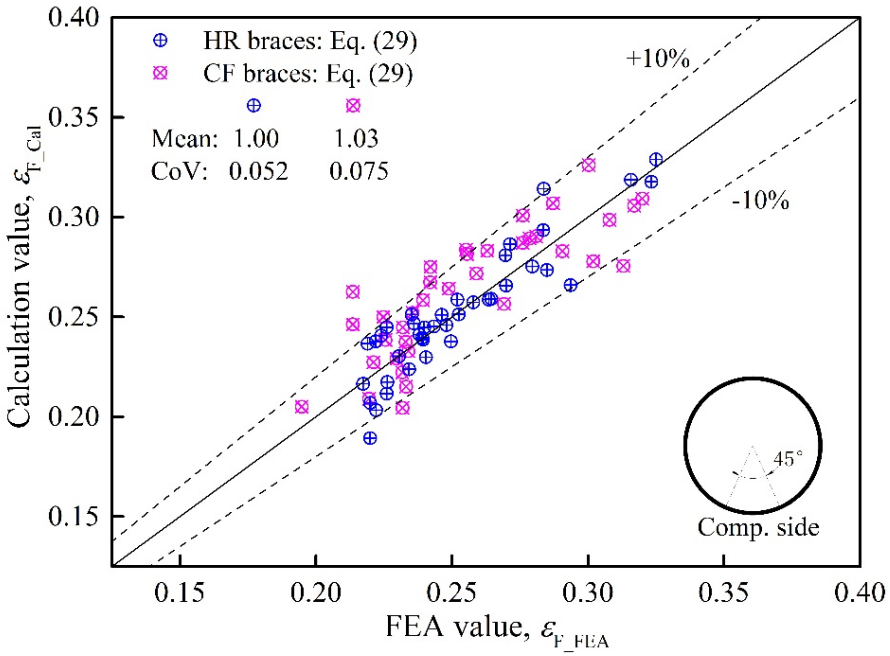
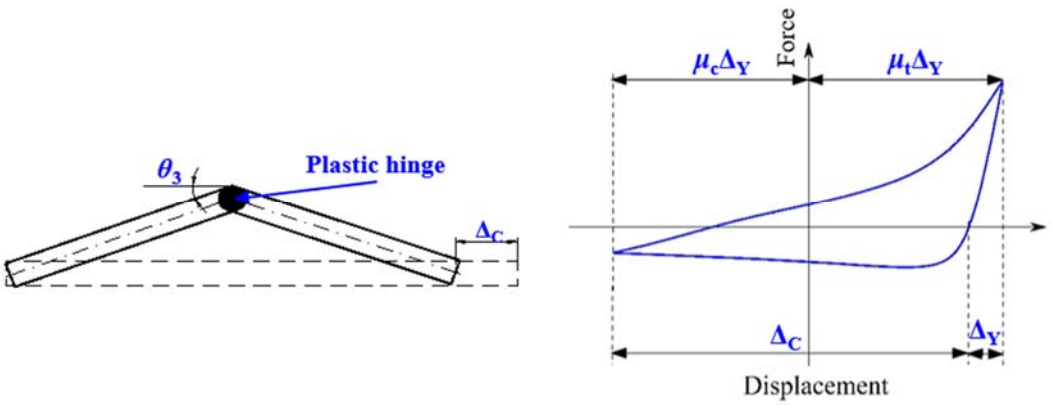
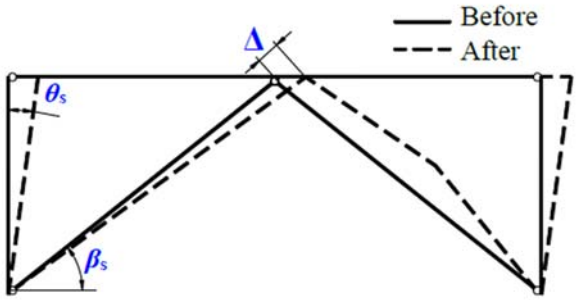


Fig. 21 Comparison of maximum compressive strain prior to fracture between calculation and FEA results

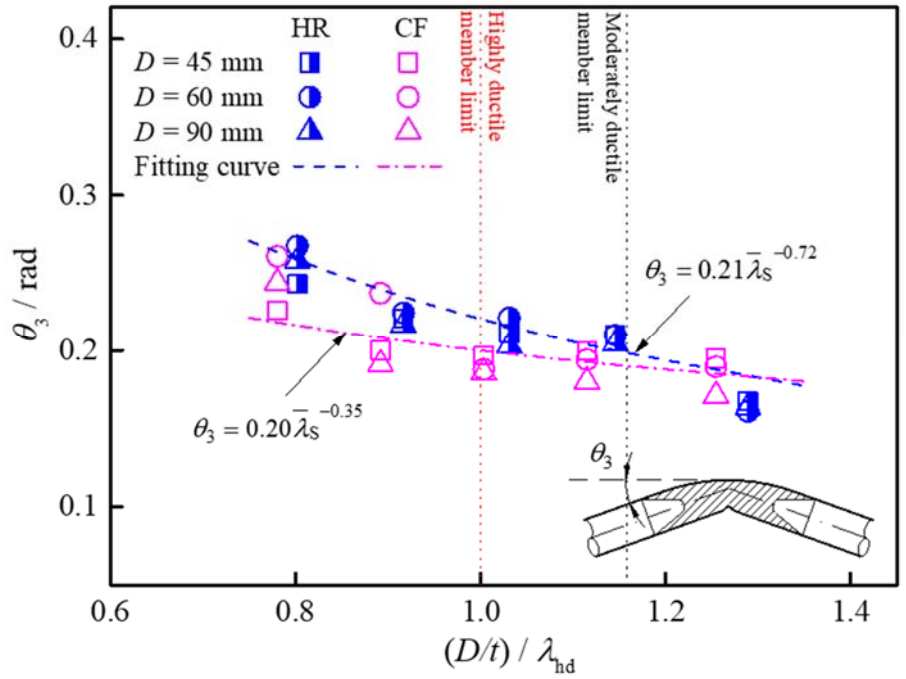


a) Plastic hinge model

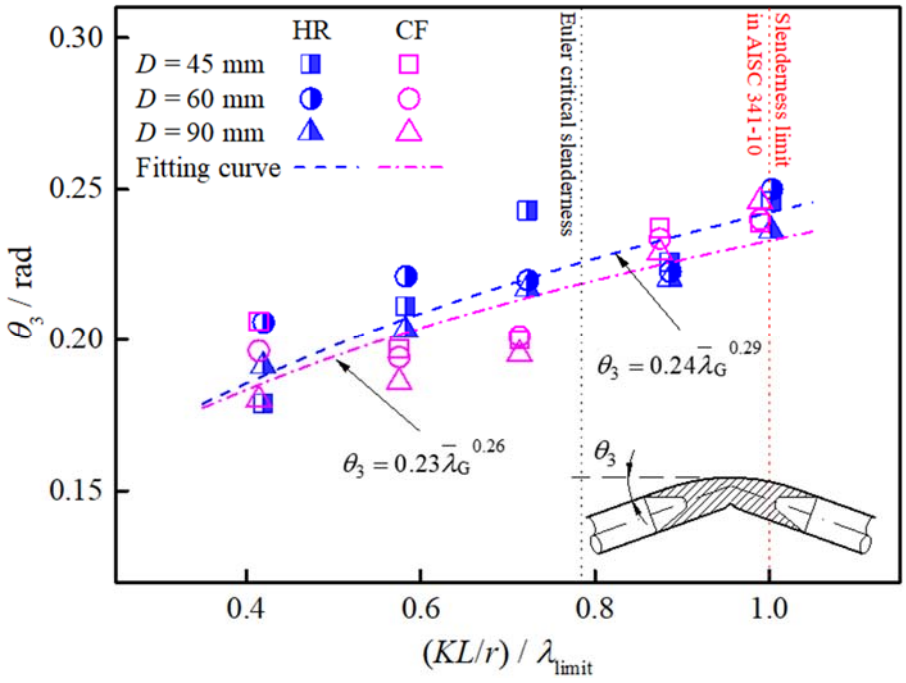


(b) One-story chevron braced frame [2]

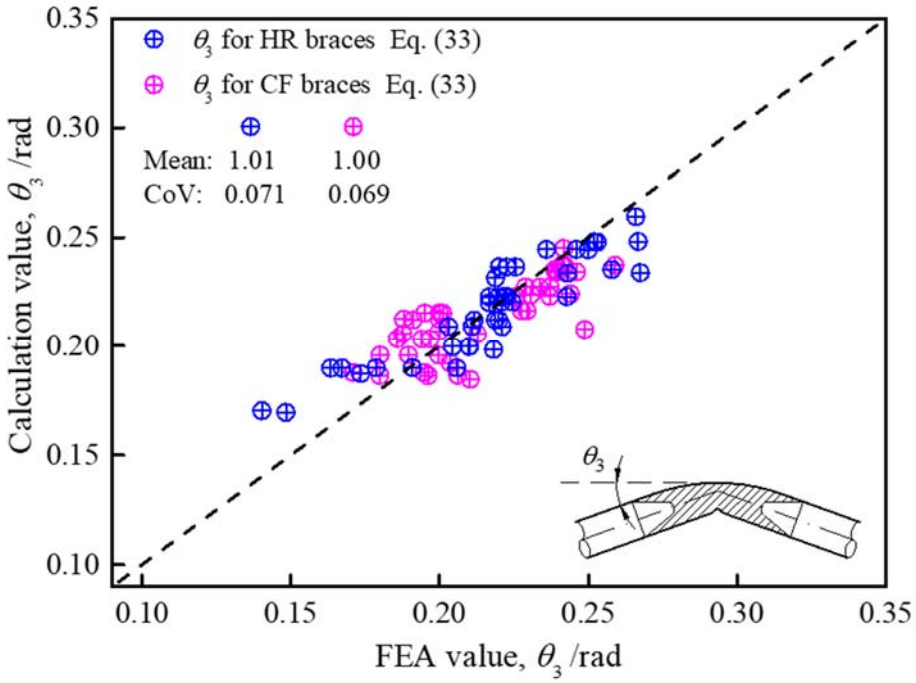
Fig. 22 Schematic illustration of simplified approach to evaluate the story drift angle in a one-story Chevron braced frame and plastic hinge model for brace (CHS)



(a) $KL/r = 50$, $\bar{\lambda}_S = \dfrac{D/t}{\lambda_{hd}}$

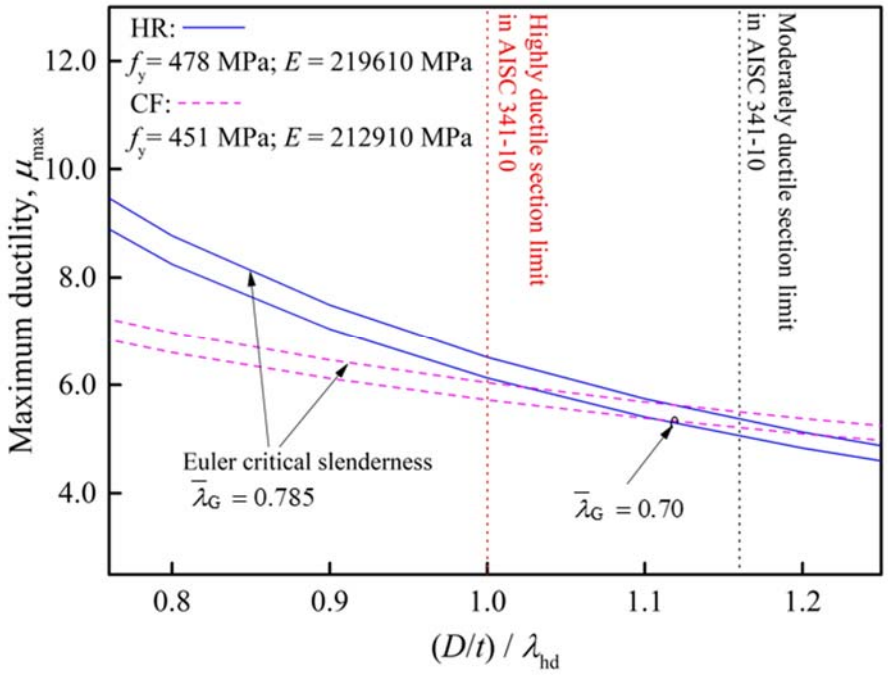


(b) $D/t = 18$, $\bar{\lambda}_G = \dfrac{KL/r}{\lambda_{limit}}$

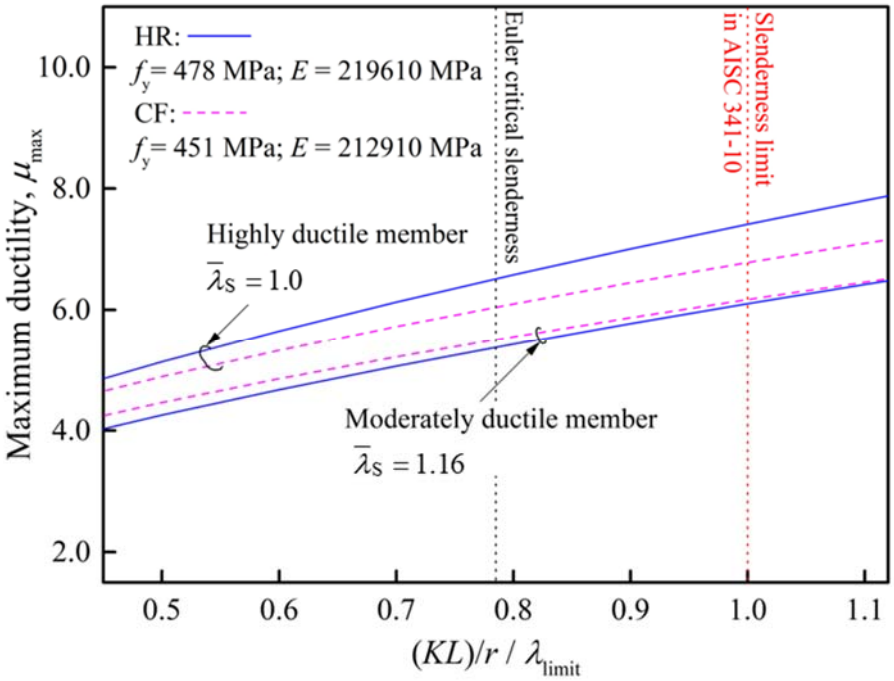


(c) Comparison between calculation and FEA results

Fig. 23 Global angle parameter, θ_3 at maximum compressive displacement prior to fracture

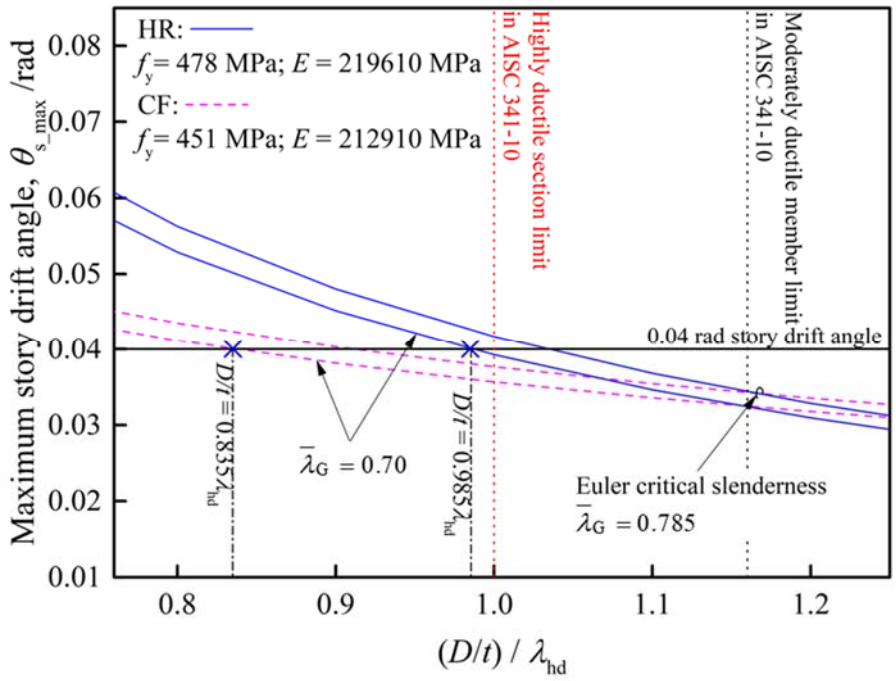


(a) Effect of D/t; $\bar{\lambda}_G = \dfrac{KL/r}{\lambda_{limit}}$

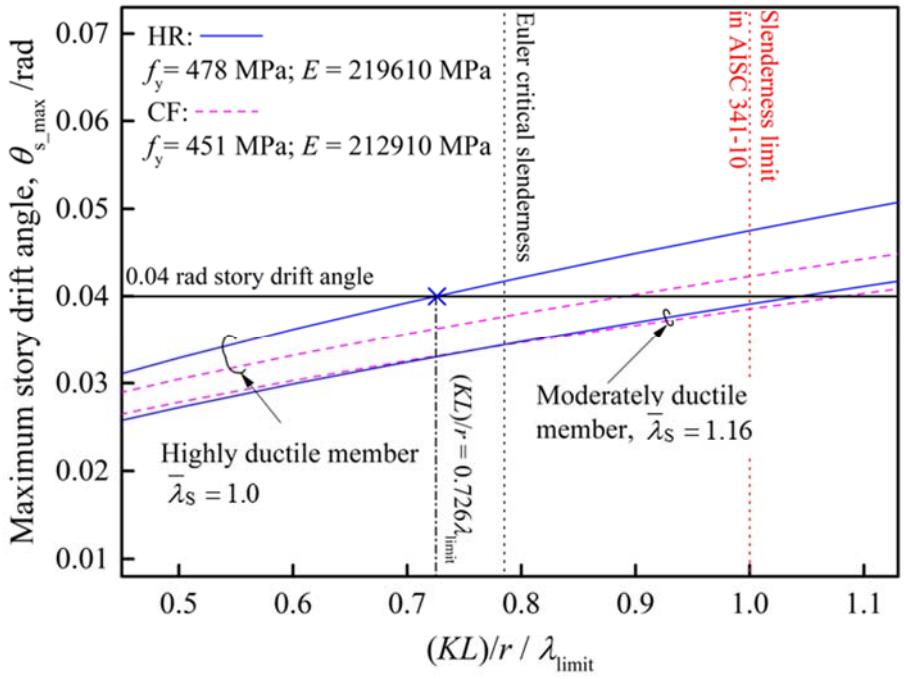


(b) Effect of KL/r; $\bar{\lambda}_S = \dfrac{D/t}{\lambda_{hd}}$

Fig. 24 Maximum allowable ductility level for brace facture



(a) Effect of D/t; $\bar{\lambda}_G = \dfrac{KL/r}{\lambda_{limit}}$



(b) Effect of KL/r; $\bar{\lambda}_S = \dfrac{D/t}{\lambda_{hd}}$

Fig. 25 Section and members limits for CHS brace based on story drift angle

Table 1. Summary of nominal dimensions and measured material properties of brace specimens

Brace type and shape/loading protocol	Label	D or B (r_s) (mm)	t (mm)	D/t or B'/t	L (mm)	$\lambda_G = KL/r$	E (GPa)	f_y (MPa)	f_u (MPa)
CHS tube/ Type A [5]	CF-H-1500	48.3	3.0	16.1	1500	65	184	499	573
	CF-H-3000	48.3	3.0	16.1	3000	131	184	499	573
	HF-H-1500	48.3	3.2	16.0	1500	65	206	415	546
	HF-H-3000	48.3	3.2	16.0	3000	131	206	415	546
Standard pipe/ Type B [2]	P1-STD5-3010	141.3	6.55	21.6	3010	63	--	326	421
	P2-STD3-3010	88.9	5.46	16.2	3010	102	--	372	464
SHS tube/ Type C [3]	40×40×3×1250-CS-CF	40.0 (3.00)	3.00	9.3	1250	41	212.9	451	502
	40×40×3×2050-CS-CF	40.0 (3.00)	3.00	9.3	2050	68	212.9	451	502
	40×40×4×2050-CS-CF	40.0 (3.50)	4.00	6.25	2050	69	201.6	410	430
	60×60×3×2050-CS-CF	60.0 (4.00)	3.00	15.3	2050	44	207.4	361	402
	40×40×3×1250-CS-HR	40.0 (1.75)	3.00	10.2	1250	41	219.6	478	555
	40×40×3×2050-CS-HR	40.0 (1.75)	3.00	10.2	2050	68	219.6	478	555
	60×60×3×2050-CS-HR	60.0 (2.75)	3.00	16.2	2050	44	215.2	458	555

Notes:

CF: cold-formed steel tube; HF: hot-finished steel tube; HR: hot-rolled steel tube; P: standard pipe; D: diameter of CHS tube; B: width of SHS tube; B': $B' = (B-2t-2r_s)/t$; t: tube-wall thickness; r_s: internal corner radius, L: brace length; K: effective length factor, r: radius of gyration.

--: Not reported.

Table 2. Comparison between test and FE results

Brace type and shape/loading protocol	Label	Imperfection used in FE models		N_{GB}		N_{LB}		N_{FI}		N_{CO}		N_{TF}	
		Global	Local	Test	FEA	Test	FEA	Test	FEA	Test	FEA	Test	FEA
CHS tube/ Type A [5]	CF-H-1500	L/2000	t/100	5	5	8	8	--	13	--	--	14	14
	CF-H-3000	L/2000	t/100	3	3	9	9	--	16	--	--	17	17
	HF-H-1500	L/2000	t/150	5	5	15	12	--	15	--	--	17	17
	HF-H-3000	L/2000	t/150	4	3	8	9	--	22	--	--	24	24
Standard pipe/ Type B [2]	P1-STD5-3010	L/1000	0.133[1]	23	23	27	23	29	26	--	--	30	26
	P2-STD3-3010	L/1000	0.070[1]	23	23	32	24	34	28	--	--	35	28
SHS tube/ Type C [3]	40×40×3×1250 -CS-CF	L/1500	t/150	4	3	8	8	--	10	10	N/A	11	N/A
	40×40×3×2050 -CS-CF*	L/2000	t/150	3	3	5	7	--	8*	10	--	11*	11*
	40×40×4×2050 -CS-CF*	L/2000	t/150	4	3	--	11	--	9*	11	--	14*	N/A
	60×60×3×2050 -CS-CF	L/2000	t/150	5	4	7	7	--	8	10	8	11	N/A
	40×40×3×1250 -CS-HR	L/1500	t/200	5	4	8	8	--	10	11	11	15	11
	40×40×3×2050 -CS-HR	L/2000	t/200	4	5	15	9	--	12	18	14	20	14
	60×60×3×2050 -CS-HR	L/2000	t/200	5	4	7	7	--	8	10	9	11	N/A

Notes:

CF: cold-formed steel tube; HF: hot-finished steel tube; HR: hot-rolled steel tube; P: standard pipe; t: tube-wall thickness; L: brace length;

N_{GB}: number of cycles to global buckling; N_{LB}: number of cycles to local buckling; N_{FI}: number of cycles to fracture initiation; N_{CO}: number of cycles to corner opening for SHS tube brace; N_{TF}: number of cycles to throughout fracture.

1: Average value of measured maximum local imperfection at different locations.

*: Specimens failed at end connections.

--: not reported/observed in tests or did not occur in FEA (Finite Element Analysis).

N/A: Convergence problem occurred.

Table 3. Parameters of plastic model used in FE models

Type		$D\times t$ or $B\times t$ mm×mm	E MPa	f_y MPa	$\sigma\|_0$ MPa	Q_∞ MPa	b	C_k MPa	γ_k
Ref. [5]	HF	48.3×3.2	206000	415	383	37.0	1.33	2266	4.1
	CF	48.3×3.0	184000	499	448	28.0	1.05	2023	3.2
Ref. [2]	Pipe	141.3×6.55	200000	326	352	89.6	7.00	3372	26.0
		88.9×5.46	200000	372	379	358.5	2.00	3447	35.0
Ref. [3]	HR[1]	60×3	215150	458	463	41.3	3.37	22670	109.8
		40×3	219610	478	463	40.5	4.92	7939	54.0
	CF-Flat[2]	60×3	207430	361	240	--	--	3414	21.3
								37413	552.7
		40×4	201640	410	319	--	--	5105	36.2
								53163	980.1
		40×3	212910	451	230	--	--	7910	43.3
								874954	6149.8
	CF-Corner[2]	60×3	200350	442	243	--	--	33930	156.2
								426507	3925.7
		40×4	210830	479	328	--	--	4402	30.6
								250688	2475.0
		40×3	196680	533	245	--	--	15612	59.9
								1256870	7051.7
Parametric study		HR[1]	219610	478	463	40.5	4.92	7939	54.0
		CF[1]	212910	451	353	37.7	0.29	47000	150.0

Notes:

1: Values (average) from cyclic coupon tests in Ref. [57];

2: Calibrated from tensile coupon tests;

Table 4. Parameters of fracture criterion and damage evolution rule used in FE models

Type		$D\times t$ or $B\times t$ mm×mm	A MPa	n	c_1	c_2 MPa	c_g	c_h	β_1	β_2	k_h
Ref. [5]	HF	48.3×3.2	625	0.090	0.12	409.8	-6	5.5	2	2	0.6 (-0.05)[1]
	CF	48.3×3.0	645	0.046	0.12	429.8	-6	5.5	2	2	0.6
Ref. [2]	Pipe	141.3×6.55	723	0.201	0.12	315.8	-6	5.5	2	2	0.6
		88.9×5.46	795	0.194	0.12	348.0	-6	5.5	2	2	0.6
Ref. [3]	HR	60×3	709	0.093	0.12	416.3	-6	5.5	2	2	0.6
		40×3	648	0.056	0.12	416.3	-6	5.5	2	2	0.6
	CF-Flat	60×3	502	0.058	0.12	301.5	-6	5.5	2	2	0.6
		40×4	604	0.092	0.12	322.5	-6	5.5	2	2	0.6
		40×3	568	0.054	0.12	376.5	-6	5.5	2	2	0.6
	CF-Corner	60×3	626	0.060	0.12	351.5	-6	5.5	2	2	0.6
		40×4	675	0.098	0.12	380.2	-6	5.5	2	2	0.6
		40×3	722	0.056	0.12	441.7	-6	5.5	2	2	0.6
Parametric study	HR		648	0.056	0.12	416.3	-6	5.5	2	2	0.6
	CF		568	0.054	0.12	376.5	-6	5.5	2	2	0.6

Note:

1: Value between parentheses for specimen HF-H-3000 only.

Table 5. Simulation matrix in parametric studies

Group	D mm	t mm	Cross-sectional slenderness D/t	Member slenderness KL/r, $K = 0.5$
HR	45	2, 2.25, 2.5, 2.8, 3.2	22.5, 20, 18, 16, 14	36, 50, 62, 76, 86
	60	2.67, 3, 3.33, 3.75, 4.29	22.5, 20, 18, 16, 14	36, 50, 62, 76, 86
	90	4, 4.5, 5, 5.6, 6.4	22.5, 20, 18, 16, 14	36, 50, 62, 76, 86
CF	45	2, 2.25, 2.5, 2.8, 3.2	22.5, 20, 18, 16, 14	36, 50, 62, 76, 86
	60	2.67, 3, 3.33, 3.75, 4.29	22.5, 20, 18, 16, 14	36, 50, 62, 76, 86
	90	4, 4.5, 5, 5.6, 6.4	22.5, 20, 18, 16, 14	36, 50, 62, 76, 86

Table 6. Parameters of proposed models

Group	θ_1			θ_2			θ_3			L_{H_G}			L_{H_L}	
	$A_{\theta 1}$	$B_{\theta 1}$	$C_{\theta 1}$	$A_{\theta 2}$	$B_{\theta 2}$	$C_{\theta 2}$	$A_{\theta 3}$	$B_{\theta 3}$	$C_{\theta 3}$	A_{H_G}	B_{H_G}	C_{H_G}	A_{H_L}	B_{H_L}
HR	0.220	-1.327	1.054	0.537	-0.856	-1.989	0.248	-0.722	0.286	0.041	0.853	-1.200	0.524	1.426
CF	0.238	-0.987	1.267	0.463	-0.435	-3.674	0.235	-0.346	0.260	0.043	0.898	-1.192	0.376	3.549